Heat transfer model for moving packed-bed particle-to-sCO_2 heat exchangers integrated with metal foams

Ashreet Mishra[1], Prashant Singh[2], Like Li[1,*]

[1]Department of Mechanical Engineering, Mississippi State University, Mississippi State, MS 39762, USA
[2]Department of Mechanical, Aerospace and Biomedical Engineering, University of Tennessee, Knoxville, TN 37996, USA

*Corresponding author: likeli@me.msstate.edu

ABSTRACT

Particle-to-supercritical carbon dioxide (sCO_2) heat exchangers (HXs) play a vital role in coupling heat transfer fluid (HTF) from high-temperature thermal receivers to power cycle working fluids (WF). Heat transfer enhancement is essential for adopting particle-based moving packed-bed heat exchangers (MPBHXs) in next-generation thermal energy storage (TES) systems, as MPBHXs usually exhibit low particle bed-to-wall heat transfer coefficients. High-porosity metal foams have shown their effectiveness in heat transfer enhancement. This work presents a continuum heat transfer model to demonstrate the heat transfer enhancement in MPBHXs when the particle bed channel is filled with high porosity metal foams compared to open channel MPBHXs. The presence of metal foams increases the effective thermal conductivity in the particle channel and enhances the interstitial heat transfer coefficient between the moving particle bed and the stationary metal foams. The present model considers coupled two-dimensional (2D) heat transfer in the particle channel with metal foams and 1D heat transfer in the sCO_2 channel and the dividing wall. The temperature profiles for the particle bed, metal foam, dividing wall, and sCO_2 stream, as well as the local heat flux profiles between those, are studied in detail for various foam porosities, from which the particle bed-to-wall heat transfer coefficient, overall heat transfer coefficient, and total heat transfer rate for the MPBHX are determined. The effects of major MPBHX design and operating parameters on the particle bed-to-wall heat transfer coefficient and overall heat exchange capacity are thoroughly examined; thus, the MPBHX performance improvement with metal foams is quantified for each case. The present heat transfer model can provide valuable insights into the metal-foam MPBHX design and optimization, scale-up, and operating parameters selection.

Keywords: moving packed bed heat exchanger; metal foams; particle-based CSP; thermal energy storage; supercritical CO_2.

1. Introduction

Renewable sources of electricity generation like concentrated solar power (CSP), wind energy, and hydro energy can reduce the dependence on fossil fuels [1–3]. They also offer the benefits of limited environmental pollution, abundant availability of resources, diversification in energy portfolio, and contribution to economic growth, so including them in the energy grid is paramount [4]. However, renewable energy sources are often associated with inherent intermittency, low efficiency, and high initial startup costs [5]. Therefore, significant efforts have been made towards addressing the above challenges [6]. To tackle the intermittent nature of solar energy, thermal energy storage (TES) is a widely used approach that enables flexible power production. Three major pathways have been outlined by the U.S. Department of Energy (DOE) for Generation 3 (Gen3) CSP systems for TES, which are molten-salt, falling-particle, and gas-phase pathways to reach levelized cost of electricity (LCOE) of $0.05/kWh to achieve a cost-competitive CSP-based power generation [7].

In comparison with molten-salt and gas-phase pathways, particle-based TES systems are advantageous due to their ability to operate at high temperatures, low energy storage cost, and cyclic stability [8,9]. Furthermore, particle-based solar receivers can be coupled with the sCO_2 Brayton cycle via a heat exchanger, which is critical to obtaining high power cycle efficiencies > 50% [10]. Based on the selection criteria of particle bed-to-wall heat transfer coefficient, cost, structural reliability, inspection ease, manufacturability, parasitic heat losses, transient operation, corrosion, and scalability, Ho et al. [9] presented a case study on three different types of heat exchangers (HXs) which included (a) shell-and-plate HX, (b) shell-and-tube HX, and (c) fluidized bed HX, that are suitable for particle-sCO_2 heat transfer. Ho et al. [9] concluded that the shell-and-plate HX and the shell-and-tube HX are better than the fluidized bed HX on cost, parasitic heat loss, manufacturability, corrosion, and transient operation aspects. In contrast, the fluidized bed HX was better regarding heat transfer coefficient, inspection ease, scalability, and structural reliability. Therefore, the shell-and-plate moving packed bed HX (MPBHX) was identified as a low-cost and robust design for particle-sCO_2 HX.

Various numerical, experimental, and analytical studies have investigated design and parametric variations for shell-and-plate MPBHXs. Isaza et al. [11] developed an analytical

solution for counter-current/co-current particle-fluid HX using Laplace transforms and expansion theorem. The non-dimensionalized temperature profiles for the particle bed and WF are presented based on the heat capacitance ratio (*C*), Biot number (*Bi*), and number of transfer units (*NTU*) of the HX. Albrecht and Ho [12] developed a 2D steady-state heat transfer model to determine the particle bed-to-wall heat transfer coefficient for a counterflow shell-and-plate moving packed bed-sCO_2 HX. The effects of particle diameter and packed bed channel spacing were studied on the particle bed-to-wall heat transfer coefficient. The overall heat transfer coefficient decreased from 208 W/m^{2}K to 139 W/m^{2}K, with an increase in particle diameter from 50 μm to 750 μm. Similarly, increasing the packed bed channel spacing from 3 mm to 9 mm also decreased the overall heat transfer coefficient from 315 W/m^{2}K to 128 W/m^{2}K. High near-wall thermal resistance and low particle bed thermal conductivity were identified as significant drawbacks, and the study suggested the usage of thin channels for higher heat transfer.

Albrecht and Ho [13] also developed a steady-state reduced order model for a multi-bank counterflow shell-and-plate moving packed bed-sCO_2 HX to investigate the design considerations and performance limitations of MPBHX. An optimal working configuration of the HX was determined after parametrically studying the HX geometry and particle properties, which showed that overall heat transfer coefficients of 400 W/m^{2}K can be obtained. An LCOE analysis also revealed that the DOE cost targets could be achieved if the sCO_2 microchannels could be produced at < \$2,400 m^{-2}. Fang et al. [14,15] conducted 2D heat transfer and fluid flow simulations in COMSOL for a counterflow particle-sCO_2 HX and integrated neural networks into the model to explore various control strategies for transient operation. Particle flow velocity, channel width, and particle thermal conductivity were determined to be the most influential parameters for MPBHX. An empirical correlation was developed for the particle bed-to-wall heat transfer coefficient and the particle flow properties based on the Nusselt (*Nu*) number. Albrecht et al. [16–18] tested a 100 kW_t HX prototype for a MPBHX at intermediate load and temperatures < 500ºC, and an overall heat transfer coefficient of 50 – 80 W/m^{2}K was obtained. The low overall heat transfer coefficient obtained experimentally shows the need for heat transfer enhancement in MPBHX to significantly enhance the heat transfer coefficient and total heat transfer. Heat transfer enhancements such as flow through tube banks have been explored by Guo et al. [19] and Torrijos et al. [20] to disrupt the temperature boundary layer and decrease the near-wall resistance/penetration thermal resistance to increase the heat transfer coefficient. Particle agitation

in granular flow has also been explored by Jiang et al. [21], which increases the specific heat transfer surface area and turbulence in the boundary layer and enhances heat transfer in granular flows. However, the drawbacks of the proposed methodology were the parasitic heat losses involved and the high complexity of the operation. Nguyen et al. [22] utilized fins to enhance the heat transfer in granular flow by increasing the heat transfer area, and Chase et al. [23] implemented binary particle mixtures to increase the effective thermal conductivity and packing fraction of particles of the granular flow, which led to an enhancement in the particle bed-to-wall heat transfer coefficient.

Although some enhancements to MPBHX/granular flows exist which employ passive/active methods to improve heat transfer, there is a demand for a straightforward approach to enhance heat transfer without parasitic energy losses while providing ease of operation and system integration. Metal foams have been traditionally used in various heat exchangers, electrochemical fuel cells, solar receivers, printed circuit microchannels, heat sinks, and chemical reactors due to their inherent fluid mixing, high thermal conductivity, interstitial heat transfer, and high surface area [24–33]. Ying et al. [34] numerically investigated the thermal behavior of partially filled metal foam phase change materials (PCM) through natural convection. Optimal filling configuration was determined for latent heat TES, where a filling height ratio of 0.75 can increase the heat storage capacity by 7.47% and save metal foam material by 25%. Schampheleire et al. [35] experimentally studied buoyance-driven flows in open-cell aluminum heat sinks. Effects of the bonding method, foam height, and pore density were studied, and it was found that foam height and pore density can enhance heat transfer by 32% and 25%, respectively. Also, Nusselt number versus Raleigh number correlations were proposed for two metal foam pore density values. He et al. [36] explored the addition of gradient metal foams and magnetic fields to improve TES performance in PCM. The solidification and TES storage rate was enhanced by 18.2% and 23.1%, respectively, due to the magnetic field while simultaneously augmenting the melting process. Zhao et al. [37] investigated TES using PCM with embedded metal foams for thermal enhancement through natural convection in metal foams. The presence of metal foam increased the overall heat transfer rate by 3-10 times and reduced the solidification time by more than half compared to PCM-only operation. Liang et al. [38] developed a novel-latent heat TES device with a metal foam composite structure/heat pipe. A validated 3D model was used to predict the heat transfer performance of the charging and discharging cycles of the TES. The copper metal foam was found

to perform better than other devices and conduction/natural convection were the major identified modes of heat transfer. Zhao and Wu [39] compared TES using PCMs for metal foam, expanded graphite, and PCM-only modes of operation under natural convection. Metal foams and expanded graphite improved heat transfer performance, with the metal foam mode of operation showing the best performance.

As shown in previous examples of metal foam thermal enhancement with natural convection, forced convection can also be a viable option to enhance heat transfer. Tian et al. [40] numerically assessed the pressure drop and heat transfer performance of porous baffles and fins compared to solid baffles in shell-and-tube HXs. Compared to traditional baffles, pressure drop performance was enhanced by 65%, and heat transfer performance was increased by 92.14%. Artificial neural network training obtained an optimal heat transfer of 4.380 kW. Alawwa et al. [41] compared the thermohydraulic performance of additively manufactured (AM) heat sinks to traditional fin heatsinks. Overall, 12.9% heat transfer enhancement at higher flow rates and 40 times lower pressure losses are obtained in AM heatsinks compared to fins. Guo et al. [42] developed a novel hybrid fins/metal foam structure to experimentally study the TES for bare tube, fin, metal foam, and fin/metal foam hybrid. Compared to the bare tube, the fin/metal foam hybrid structure reduced PCM melting time by 83.35% and increased the temperature response rate by 529.10%. In addition, metal foams showed higher temperature uniformity than bare tube, fins, and fins/metal foam hybrid. Saedodin et al. [43] evaluated a flat-plate solar collector's flow and heat transfer performance with porous copper metal foam. The numerical and experimental results indicated that thermal efficiency increased by 18.5%, and the *Nu* increased by 82% in the presence of metal foams. In contrast, the authors found that the increase in pressure drop due to metal foams was not significant enough to require higher operating power. Customizable metal foams in AM metal foams can be curated to selectively design metal foams with desired heat transfer and fluid flow characteristics [44]. Metal foams can enable high interstitial heat transfer coefficients between the foam structure and the moving fluid through them, which can be leveraged to enhance heat transfer in granular flows [45–48].

According to the literature review above, particle-based MPBHXs exhibit low particle bed-to-wall heat transfer coefficients due to near-wall resistance and low particle bed intrinsic thermal conductivity. There exists a need for heat transfer enhancement in MPBHXs, which can be easy

to integrate into the present infrastructure, have a simple mode of operation, have low parasitic heat losses, and enhance the particle bed-to-wall heat transfer coefficient. Granular flow through metal foams can be a proposition where the particle bed-to-wall heat transfer in MPBHXs can be enhanced with increases in both the interstitial heat transfer coefficient and the effective thermal conductivity of the bed [47,48]. Therefore, a comprehensive understanding of the coupled flow and heat transfer in MPBHXs with metal foams is necessary to quantitatively evaluate their applicability and improvement metrics.

This study aims to address the above knowledge gap by proposing a continuum heat transfer model to demonstrate heat transfer enhancement in MPBHXs when the particle bed channel is filled with high porosity metal foams compared to a geometrically similar open channel (absence of metal foams). The heat transfer model considers 2D heat transfer in the particle channel and 1D heat transfer in the sCO_2 channel and the dividing wall, coupled via thermal resistance networks. The developed heat transfer model is verified analytically and numerically with open channel MPBHX and forced convection in metal foam channel cases, and used to study the temperature profiles and local heat flux profiles from which the MPBHX thermal performance is determined. In addition, the effects of critical operating parameters on the heat transfer performance are also elucidated. The rest of the paper is organized as follows. Section 2 describes the MPBHX system and numerical model. Then, the model verification is shown in Section 3, and Section 4 presents the detailed results and discussion. Finally, the concluding statements are given in Section 5.

2. Model Description

2.1. HX configuration and model assumptions

The schematics of the counterflow shell-and-plate particle-to-sCO_2 MPBHXs with an open channel and a channel filled with metal foams for falling particle flow are shown in Fig. 1 (a, b), respectively. An actual MPBHX will consist of multiple repeating channels, and only one channel is depicted in Fig. 1. The width of the particle channel is W_{bed}, the height is H, and the dividing wall thickness is t_w. The sCO_2 channel with width W_g operates in the counter current flow setting and carries sCO_2 out of the HX to a Brayton cycle [49]. In this model, the moving packed bed of falling particles is the HTF that flows through the metal foam under gravity, and the metal foam structure is stationary, acting as the heat transfer enhancement medium for the MPBHX. For

modeling purposes, only half the channel width is considered for both the particle channel and sCO_2 channel due to geometrical symmetry, as seen in Fig. 1 (a, b).

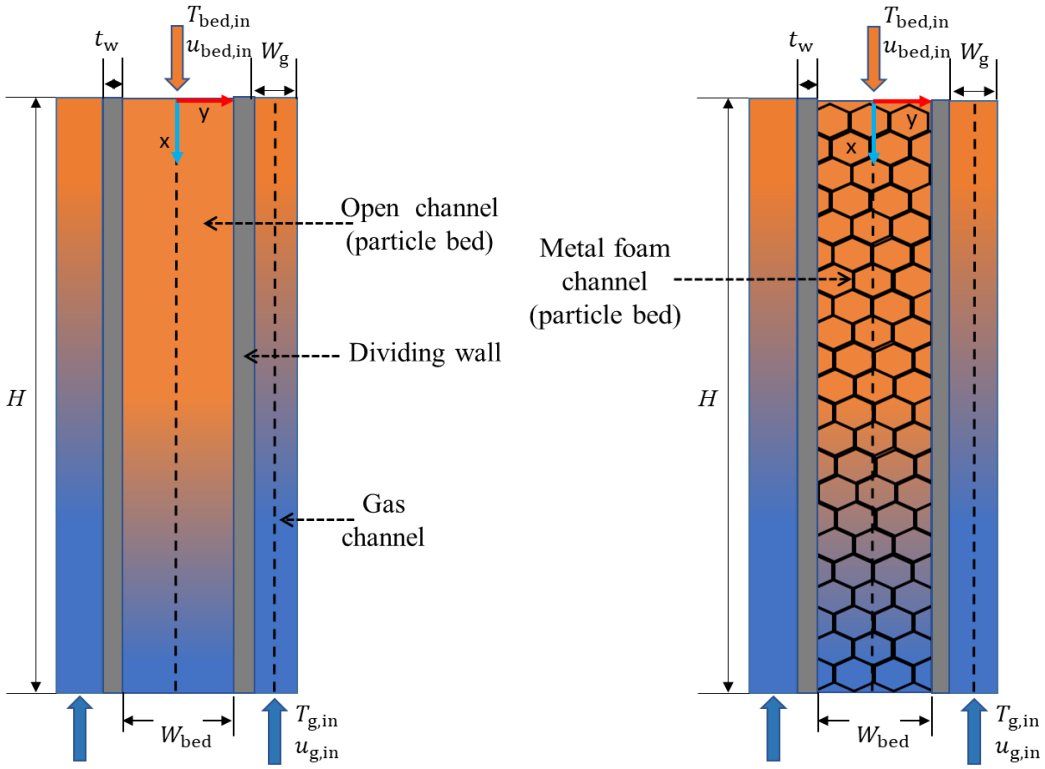

(a) **(b)**

Fig. 1. Schematic depiction of two particle-to-sCO_2 HX designs with (a) an open channel for moving particle bed and (b) a particle bed channel filled with high-porosity metal foams (dashed lines represent symmetry lines in both domains).

The thermal model assumptions are as follows:

1. Steady-state process.
2. Plug flow is assumed for the particle bed and sCO_2 flow [19,50].
3. The solid particles and interstitial air are in local thermal equilibrium [11,12] and are treated as a single continuous medium (particle bed) or one-way coupling.
4. The thermophysical properties (density, specific heat capacity, and thermal conductivity) of particle bed, metal foam, wall, and the sCO_2 are evaluated at the mean of the particle bed and sCO_2 inlet temperatures (662.5ºC) and are assumed to be constant [12,19,51].
5. For heat transfer in the particle bed, convection dominates in the axial *x*-direction and conduction dominates in the *y*-direction [11,20].

6. For the sCO_2 flow, 1D heat transfer in the *x*-direction only is assumed.
7. The metal foam is assumed to have uniform porosity throughout the channel without manufacturing defects [29,45].
8. Viscous dissipation and radiation effects (for particle diameter < 550 μm) are considered negligible [12,13,51].

2.2. Model development

The model solves the coupled heat transfer problem between a moving packed bed flowing through a metal foam and sCO_2 in counterflow shell-and-plate HX. As summarized in Table 1, the 2D steady-state energy conservation equations for the moving particle bed and the stationary metal foam structure are given in Eqs. (1, 2), and the 1D steady-state energy conservation equations for the wall and sCO_2 are given in Eqs. (3, 4), respectively [11,12,52]. A local thermal non-equilibrium approach is used to model the heat transfer between the metal foam and the particle bed owing to a high thermal conductivity difference between the materials [53,54].

Table 1. Governing equations.

Energy balance for particle bed

$$\rho_{\mathrm{bed}} c_{\mathrm{p,bed}} u_{\mathrm{bed}} \frac{\partial T_{\mathrm{bed}}}{\partial x} = k_{\mathrm{bed,eff}} \frac{\partial^2 T_{\mathrm{bed}}}{\partial y^2} + h_{\mathrm{v}} \left(T_{\mathrm{mf}} - T_{\mathrm{bed}} \right) \tag{1}$$

Energy balance for metal foam

$$k_{\mathrm{mf,eff}} \frac{\partial^2 T_{\mathrm{mf}}}{\partial x^2} + k_{\mathrm{mf,eff}} \frac{\partial^2 T_{\mathrm{mf}}}{\partial y^2} + h_{\mathrm{v}} (T_{\mathrm{bed}} - T_{\mathrm{mf}}) = 0 \tag{2}$$

Energy balance for dividing wall

$$k_{\mathrm{w}} \frac{\partial^2 T_{\mathrm{w}}}{\partial x^2} + \frac{1}{R_{\mathrm{g}} t_{\mathrm{w}}} \left(T_{\mathrm{g}} - T_{\mathrm{w}} \right) + \frac{1}{R_{\mathrm{bed}} t_{\mathrm{w}}} \left(T_{\mathrm{bed}} \left(x, 0.5 W_{\mathrm{bed}} \right) - T_{\mathrm{w}} \right) + \frac{1}{R_{\mathrm{mf}} t_{\mathrm{w}}} \left(T_{\mathrm{mf}} \left(x, 0.5 W_{\mathrm{bed}} \right) - T_{\mathrm{w}} \right) = 0 \tag{3}$$

Energy balance for sCO_2

$$\rho_{\mathrm{g}} c_{\mathrm{p,g}} u_{\mathrm{g}} \frac{dT_{\mathrm{g}}}{dx} = \frac{2 q_{\mathrm{wg}}}{W_{\mathrm{g}}} \tag{4}$$

In Eqs. (1-4), T is the local volume-averaged temperature, the subscript "bed' denotes the particle bed, "mf" denotes metal foam, "g" denotes sCO_2, and "w" denotes the dividing wall, ρ is the density, c_{p} is the specific heat capacity, k is the thermal conductivity, u_{bed} is the particle bed

superficial velocity, and u_g is the sCO_2 velocity. The local heat flux (q) from the particle channel to the dividing wall and from the wall to the sCO_2 channel are described in Table 2. The specific thermal resistances (R) and thermal conductivities (k) are summarized in Table 3. The thermo-physical properties of particles used in this study are adopted from Albrecht and Ho [12], metal foam is made of Stainless Steel (SS-420), and sCO_2 properties are taken from Span and Wagner [55] and the NIST handbook [56].

Table 2. Local heat flux components.

Wall-to-sCO_2

$$q_{wg}(x) = q_{bed}(x) + q_{mf}(x) \tag{5a}$$

Particle bed-to-wall

$$q_{bed}(x) = -k_{bed,eff}\left.\frac{\partial T_{bed}}{\partial y}\right|_{(x,0.5W_{bed})} = \frac{1}{R_{bed}}\left[T_{bed}(x,0.5W_{bed}) - T_w(x)\right] \tag{5b}$$

Metal foam-to-wall

$$q_{mf}(x) = -k_{mf,eff}\left.\frac{\partial T_{mf}}{\partial y}\right|_{(x,0.5W_{bed})} = \frac{1}{R_{mf}}\left[T_{mf}(x,0.5W_{bed}) - T_w(x)\right] \tag{5c}$$

In Table 3, Eqs. (6, 9, & 10) define the specific thermal resistances. The near-wall resistance model is adopted from Botterill and Denloye [57], where d_p in Eq. (7) is the particle diameter. Yagi and Kunni [58] and Denloye and Botterill [59] have proposed a well-adapted correlation [12,60] for modeling near-wall particle bed effective thermal conductivity as given in Eq. (8), where Φ_{nw} is the effective thickness of the fluid film. The particle bed thermal conductivity in an open channel is given in Eq. (11) where k_{air} is the air thermal conductivity, k_p is the solid particle thermal conductivity, β, γ, and φ are constants taken from Yagi and Kunni [58], and ε_{bed} is the porosity of the particle bed. The overall metal foam thermal conductivity for the metal foam Octet structure with the particle bed treated as the fluid phase can be obtained using the correlation developed by Wang et al. [45] in Eq. (12), where k_{tot} is the overall thermal conductivity of the porous structure, including connected metal foam fibers and particle bed between the fibers, k_{mf} is the metal foam fiber thermal conductivity, and ϕ_{mf} is the porosity of the metal foam. The effective particle bed thermal conductivity ($k_{bed,eff}$) and the effective metal foam thermal conductivity ($k_{mf,eff}$)

are defined in Eqs. (13, 14) respectively. The thermophysical metal foam properties and porosities are mentioned in Table 4.

Table 3. Constitutive equations for specific thermal resistance and thermal conductivity.

Particle bed-to-wall specific thermal resistance

$$R_{\mathrm{bed}} = R_{\mathrm{nw}} + \frac{t_{\mathrm{w}}}{2k_{\mathrm{w}}} \tag{6}$$

Near-wall specific thermal resistance [57]

$$R_{\mathrm{nw}} = \frac{d_{\mathrm{p}}}{2k_{\mathrm{bed,eff}}^{\mathrm{nw}}} \tag{7}$$

Near-wall particle bed effective thermal conductivity [58,59]

$$k_{\mathrm{bed,eff}}^{\mathrm{nw}} = k_{\mathrm{air}}\left(\varepsilon_{\mathrm{nw}} + \frac{1-\varepsilon_{\mathrm{nw}}}{2\Phi_{\mathrm{nw}} + \frac{2k_{\mathrm{air}}}{3k_{\mathrm{p}}}}\right) \tag{8}$$

sCO_2-to-wall specific thermal resistance

$$R_{\mathrm{g}} = \frac{1}{h_{\mathrm{sCO_2}}} + \frac{t_{\mathrm{w}}}{2k_{\mathrm{w}}} \tag{9}$$

Metal foam-to-wall specific thermal resistance

$$R_{\mathrm{mf}} = \frac{t_{\mathrm{w}}}{2k_{\mathrm{w}}} \tag{10}$$

Thermal conductivity of particle bed [58]

$$k_{\mathrm{bed}} = \frac{k_{\mathrm{air}}\beta(1-\varepsilon_{\mathrm{bed}})}{\gamma\frac{k_{\mathrm{air}}}{k_{\mathrm{p}}} + \varphi} \tag{11}$$

Thermal conductivity of metal foam [45]

$$\frac{k_{\mathrm{tot}}}{k_{\mathrm{mf}}} = 0.7397\phi_{\mathrm{mf}}^2 + \left(\frac{k_{\mathrm{bed}}}{k_{\mathrm{mf}}} - 1.7397\right)\phi_{\mathrm{mf}} + 1 \tag{12}$$

Effective thermal conductivity of particle bed

$$k_{\mathrm{bed,eff}} = \phi_{\mathrm{mf}} k_{\mathrm{bed}} \tag{13}$$

Effective thermal conductivity of metal foam

$$k_{\mathrm{mf,eff}} = k_{\mathrm{tot}} - \phi_{\mathrm{mf}} k_{\mathrm{bed}} \tag{14}$$

Table 4. Metal foam thermophysical properties.

Parameter	Value	Reference

k_{mf} (W/m^{2}K)	20.80	[47]
ϕ_{mf}	0.70 / 0.80 / 0.88	[29,45]
d_{fiber} (mm)	2.50 / 2.0 / 1.50	[29,45]

The remaining constitutive equations are described in Table 5, where a is the contact surface curvature in Eq. (15) [57]. The convective heat transfer coefficient due to sCO_2 flow is given by Gnielinski correlation [61] in Eq. (16), where Re_{D_h} is the hydraulic diameter-based Reynolds number, Pr is the Prandtl number, and Eq. (17) gives the Darcy friction factor [62]. The particle bed-to-metal foam volumetric heat transfer coefficient is obtained from Tzeng and Jeng [63] for flow through metal foams, where Pr_{bed} is the bed Prandtl number defined in Eq. (20), and Re_d is the metal foam fiber diameter-based Reynolds number for particle bed flow. The constants σ (0.0037 for ϕ_{mf} = 0.70, 0.00276 for ϕ_{mf} = 0.80, and 0.0026 for ϕ_{mf} = 0.88) and λ = 0.932 for ϕ_{mf} = 0.70, 0.80, and 0.88 in Eq. (18) are porosity dependent constants obtained from [63]. The particle bed viscosity is given by Eq. (19), where φ_{bed} is the particle bed packing fraction, χ and c are constants given in [64].

Table 5. Constitutive correlations for flow and heat transfer in the particle bed, metal foam, and sCO_2 channels.

Near-wall voidage [57]

$$\varepsilon_{nw} = 1 - \frac{\left(1-\varepsilon_{bed}\right)\left(0.7293 + 0.5139\frac{d_p}{2a}\right)}{\left(1+\frac{d_p}{2a}\right)} \tag{15}$$

sCO_2 flow heat transfer coefficient [61]

$$h_{sCO_2} = \frac{D_h\left(f/8\right)\left(\mathrm{Re}_{D_h} - 1000\right)\mathrm{Pr}_{sCO_2}}{1+12.7\left(f/8\right)^{1/2}\left(\mathrm{Pr}_{sCO_2}^{2/3}-1\right)k_{sCO_2}} \tag{16}$$

Darcy friction coefficient [62]

$$f = \left(0.79\ln\left(\mathrm{Re}_{D_h}\right) - 1.64\right)^{-2} \tag{17}$$

Particle bed-metal foam volumetric heat transfer coefficient [63]

$$h_v = \frac{\sigma Re_d^{\lambda}\mathrm{Pr}_{bed}^{0.37}k_{bed}}{d_{fiber}^2} \tag{18}$$

Effective viscosity of the particle bed [64]

$$\frac{\mu_{\text{bed}}}{\mu_{\text{air}}} = e^{2.5\chi(1-\varphi_{\text{bed}})^{c}-1} \tag{19}$$

Prandtl number of the particle bed

$$\text{Pr}_{\text{bed}} = \frac{\mu_{\text{bed}} c_{\text{p,bed}}}{k_{\text{bed}}} \tag{20}$$

The boundary conditions for the governing equations (1-4) include inlet temperatures

$$T_{\text{bed}}(0,y) = T_{\text{bed,in}},\ T_{\text{g}}(H) = T_{\text{g,in}} \tag{21a}$$

and fully developed profiles at the exits; and the metal foam and dividing wall are assumed well insulated at the two ends, yielding the following

$$\frac{\partial T_{\text{bed}}}{\partial x}\Big|_{(H,y)} = 0,\ \frac{dT_{\text{g}}}{dx}\Big|_{(0)} = 0 \text{; and} \tag{21b}$$

$$\frac{\partial T_{\text{mf}}}{\partial x}\Big|_{(0,y)} = 0,\ \frac{\partial T_{\text{mf}}}{\partial x}\Big|_{(H,y)} = 0,\ \frac{dT_{\text{w}}}{dx}\Big|_{(0)} = 0,\ \frac{dT_{\text{w}}}{dx}\Big|_{(H)} = 0. \tag{21c}$$

The heat transfer evaluation metrics for MPBHXs are summarized in Table 6. The methodology to solve Eqs. (1 – 4) using boundary conditions in Eqs. (21a – 21c) and the constitutive equations (5 – 20) will be described in Section 2.3.

Table 6. Heat transfer evaluation parameters.

Particle bed-to-wall heat transfer coefficient
$h_{\text{bed,w}}(x) = \dfrac{q_{\text{bed}}(x) + q_{\text{mf}}(x)}{T_{\text{bed,avg}}(x) - T_{\text{w}}(x)}$ (22)
Average particle bed-to-wall heat transfer coefficient
$\bar{h}_{\text{bed,w}} = \dfrac{1}{H}\int_0^H h_{\text{bed,w}}(x)dx$ (23)
Overall heat transfer coefficient
$U = \left(\dfrac{1}{\bar{h}_{\text{bed,w}}} + \dfrac{t_{\text{w}}}{k_{\text{w}}} + \dfrac{1}{h_{\text{sCO}_2}}\right)^{-1}$ (24)
Total heat transfer

$$Q = UA\Delta T_{\mathrm{LMTD}} \tag{25}$$

With the log mean temperature difference (LMTD)

$$\Delta T_{\mathrm{LMTD}} = \frac{\left(T_{\mathrm{bed}}^{\mathrm{out}} - T_{\mathrm{g}}^{\mathrm{in}}\right) - \left(T_{\mathrm{bed}}^{\mathrm{in}} - T_{\mathrm{g}}^{\mathrm{out}}\right)}{\ln\left(\frac{T_{\mathrm{bed}}^{\mathrm{out}} - T_{\mathrm{g}}^{\mathrm{in}}}{T_{\mathrm{bed}}^{\mathrm{in}} - T_{\mathrm{g}}^{\mathrm{out}}}\right)} \tag{26}$$

2.3. Numerical implementation

The four partial differential equations Eqs. (1-4) are implemented with an in-house finite difference solver built in MATLAB. The particle bed and metal foam physical domains are divided into N_x number of grids in the *x*-direction and N_y number of grids in the *y*-direction, while the dividing wall and sCO_2 are divided into N_x number of grids in the *x*-direction. The convective terms in Eqs. (1, 4) are spatially discretized using a first-order upwind method, whereas the diffusive terms in Eqs. (1-3) are spatially discretized using the second-order central-difference scheme. The moving packed bed and metal foam energy conservation equations (Eqs. (1, 2)) are coupled with the gas energy conservation equation (Eq. (4)) through the wall energy equation (Eq. (3)). The solution is considered to have reached steady state when the L_2 norm error between consecutive iterations for the local particle bed temperature is less than 10^{-12}. Fig. 2 shows the solution procedure for the energy balance equations. From the temperature output, the local heat flux, heat transfer coefficients, and total heat transfer were obtained in the post-processing steps.

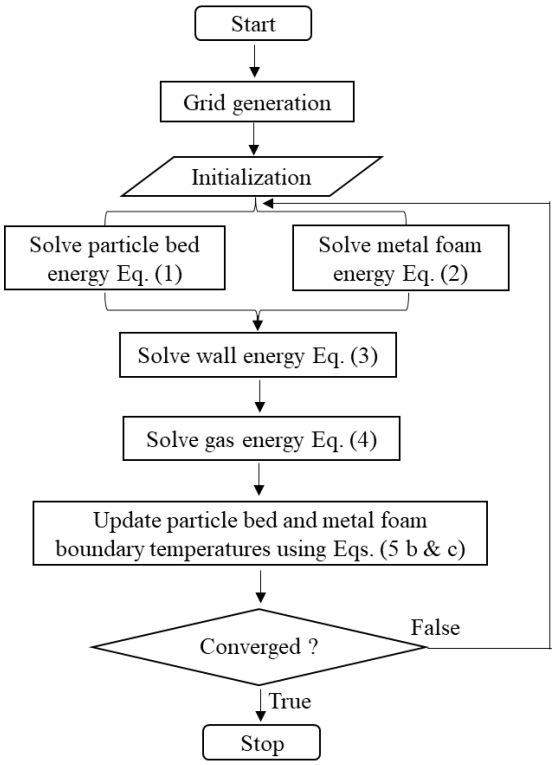

Fig. 2. Flow chart for the steady state heat transfer model.

3. Model Verification

This section verifies the applicability and accuracy of the coupled heat transfer model for MPBHXs with/without metal foams. Subsection 3.1 presents the model verification for two types of open channel counter-current MPBHXs, one with numerical solution from Albrecht and Ho [12] and the other with an analytical solution from Isaza et al. [11] for particle bed-to-sCO_2 heat exchange. And in subsection 3.2, the present model is modified to simulate the forced convection through metal foams, and the simulation results are verified with the analytical solution from Lee and Vafai [53].

3.1. Open channel MPBHX model: verification with reduced-order models and analytical solution

To verify the open channel MPBHX model, Eqs. (1, 3, and 4) are used with the metal foam components omitted. The present model is compared with Albrecht and Ho's [12] numerical solution for an open channel particle bed-to-sCO_2 MPBHX. A grid independence study is first conducted to verify the appropriate grid convergence where the sCO_2 outlet temperature from the

present model is compared with that from Albrecht and Ho [12] in Table 7 at different grid sizes based on the baseline operating parameters in Table 8, where the relative error is defined as

$$\text{R.E.} = \left| \frac{T_{\text{sCO}_2,\text{out}} - T_{\text{sCO}_2,\text{out,ref}}}{T_{\text{sCO}_2,\text{out,ref}}} \right| \times 100\% \tag{27}$$

The R.E. decreases as the grid size increases from 64×16 to 1024×256 and asymptotes around a value of 256×64. Hence, a grid size of 256×64, which sufficiently captures the heat transfer, is chosen as the grid size for the open channel case for the rest of the work. It is to be noted that the appropriate grid independence for the metal foam MPBHX will be determined in Section 4.2.

Table 7. Grid independence study for the sCO_2 outlet temperature comparison with Albrecht and Ho [12] **($T_{\text{sCO}_2,\text{out}}$ = 700 °C).**

Grid size ($N_x \times N_y$)	$T_{\text{bed,out}}$ (°C)	Relative Error (%)
64×16	693.42	0.93
128×32	695.30	0.67
256×64	696.23	0.53
512×128	696.68	0.47
1024×256	696.90	0.44

Table 8. Baseline parameters for the open channel MPBHX from Albrecht and Ho [12]**.**

Parameter	Value
H (m)	1
W_{bed} (m)	6×10^{-3}
W_g (m)	5×10^{-4}
ρ_p (kg/m^3)	3333
$c_{p,p}$ (J/kgK)	1200
ε_{bed}	0.4
k_p (W/mK)	2
d_p (m)	250×10^{-6}
t_w (m)	1×10^{-3}
k_w (W/mK)	23
$T_{\text{bed,in}}$ (°C)	775
$T_{g,\text{in}}$ (°C)	550

Next, the present model is compared with Albrecht and Ho's [12] numerical solution for an open channel particle bed-to-sCO$_2$ MPBHX. Fig. 3 (a) compares the present model's temperature profiles for the particle bed, wall, and sCO$_2$ with those in [12] based on the baseline parameters summarized in Table 8. Good agreement is observed between the two models, and the slight discrepancy is attributed to the difference in evaluating the bed thermal conductivity and wall resistance constants. In terms of local heat transfer coefficient ($h_{\text{bed,w}}$) comparison, Fig. 3 (b) shows excellent agreement in comparing $h_{\text{bed,w}}$ based on the particle bed inlet temperature, $T_{\text{bed,in}}$, (i.e., $h^{\text{in}}_{\text{bed,w}}(x)=\dfrac{q_{\text{bed}}(x)}{T^{\text{in}}_{\text{bed}}-T_{\text{w}}(x)}$), and also reasonable agreement for that based on the particle bed average temperature, $T_{\text{bed,avg}}$, (i.e., $h^{\text{avg}}_{\text{bed,w}}(x)=\dfrac{q_{\text{bed}}(x)}{T_{\text{bed,avg}}(x)-T_{\text{w}}(x)}$) with a slight difference near the outlet region observed because of the different boundary conditions used: a no-flux particle bed outlet boundary condition was used in the present model, whereas a Dirichlet boundary condition was used in Albrecht and Ho [12]. Similar verification studies have also been performed in [51,60] considering the effects of particle-particle and particle-wall radiation, where for the present d_{p} (250μm) the effects of radiation were found not pronounced.

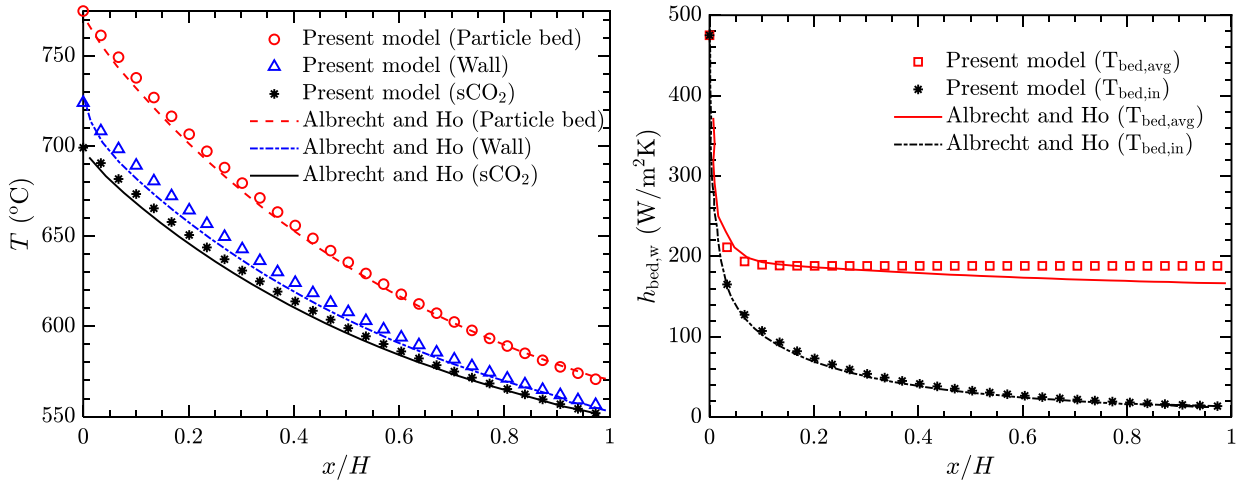

Fig. 3. Comparison of (a) simulated temperature profiles of the particle bed, dividing wall, and sCO$_2$ and (b) local particle bed-to-wall heat transfer coefficient along the axial direction with numerical data from Albrecht and Ho [12]**.**

Next, the present model is verified by comparing the streamwise temperature profiles of the particle bed and sCO$_2$ with analytical solution from Isaza et al. [11]. The non-dimensional

temperature (θ) profiles defined as $\theta_{\text{bed}} = \dfrac{T_{\text{bed}} - T_{\text{g}}^{\text{in}}}{T_{\text{bed}}^{\text{in}} - T_{\text{g}}^{\text{in}}}$ and $\theta_{\text{g}} = \dfrac{T_{\text{g}} - T_{\text{g}}^{\text{in}}}{T_{\text{bed}}^{\text{in}} - T_{\text{g}}^{\text{in}}}$ are presented in Fig. 4 for characteristic numbers at the design point from Albrecht and Ho [12], where C = 0.72, Bi = 2.13, and NTU = 7.97. A good agreement is observed between our model and the analytical solution from Isaza et al. [11].

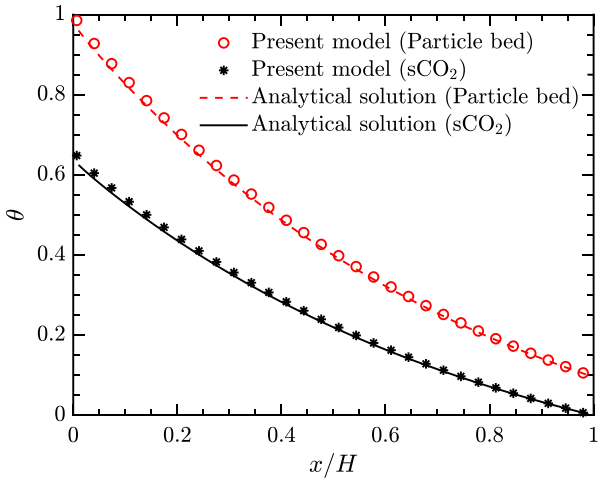

Fig. 4. Comparison of temperature profiles of particle bed and sCO_2 along the transverse directions with the analytical solution for counterflow MPBHX in Isaza et al. [11]**.**

3.2. Forced convection through metal foams: verification with analytical solution

To the best of authors' knowledge on open literature pertaining to MPBHX modeling, a particle bed-to-sCO_2 HX with metal foam introduced in the particle channel has not been modeled. We hypothesize that the moving particle bed can be treated as a moving fluid phase with effective transport properties through the metal foam structure. Hence in this section, we verify our model by simulating forced convection between a moving packed particle bed and porous medium (metal foam). The present MPBHX model is modified to match the Bi and thermal conductivity ratio $\sigma = k_{\text{mf,eff}}/k_{\text{bed,eff}}$, and a constant heat flux boundary condition is applied on the dividing wall (i.e., only the convection in the particle bed-metal form channel is simulated, and the sCO_2 channel is not included). The steady-state temperature profiles, $\theta_{\text{eff}} = \dfrac{4D_{\text{h,bed}}k_{\text{mf,eff}}\left(T - T_{\text{w}}\right)}{q_{\text{w}}}$, are compared with those obtained from the analytical solutions given by Lee and Vafai [53] for forced convection through a channel filled with porous media, where the Bi and σ were varied and the hydraulic

diameter of the channel is given by $D_{\mathrm{h,bed}} = \dfrac{2HW_{\mathrm{bed}}}{H + W_{\mathrm{bed}}}$. Our model shows good comparison with the analytical solution (Fig. 5).

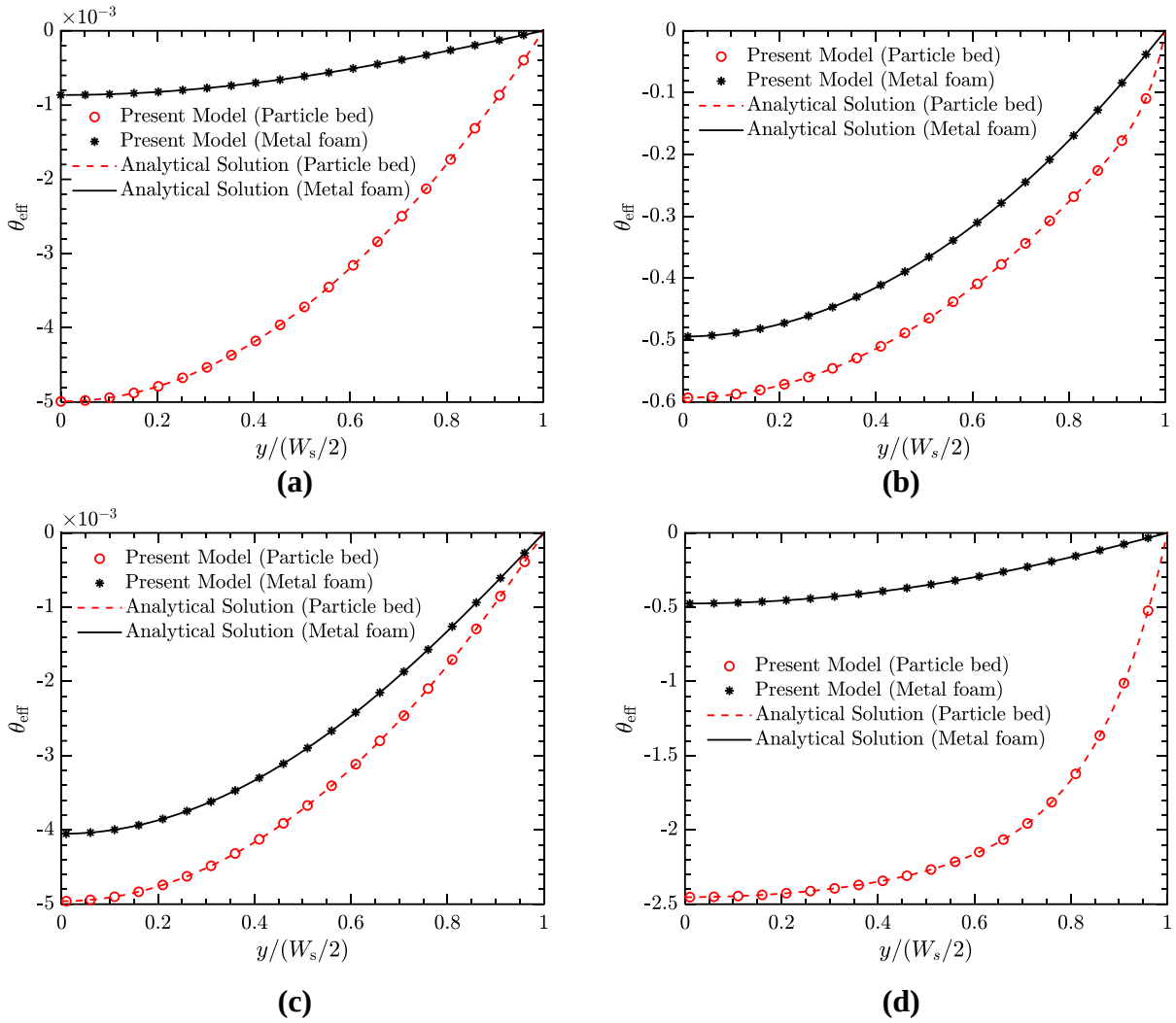

Fig. 5. Comparison of dimensionless temperature profiles of the particle bed as HTF and the metal foam structure with analytical solution from Lee and Vafai [53] **at (a) *Bi* = 0.5 and *σ* = 100, (b) *Bi* = 10 and *σ* = 0.01, (c) *Bi* = 10 and *σ* = 100, and (d) *Bi* = 0.5 and *σ* = 0.01.**

4. Results and Discussion

The verified model is used to analyze thermal enhancement due to the presence of metal foam in the particle channel, and the numerical results are presented in this section. Subsection 4.1 explains the hypothesis for heat transfer enhancement due to the presence of metal foam. Next, the temperature distributions and the particle bed-to-wall and wall-to-sCO_2 local heat flux profiles are reported for metal foam and open channel MPBHXs in Subsection 4.2. From the temperature

profiles and heat flux values, the heat transfer coefficient is obtained and discussed in Subsection 4.3, and the heat transfer performance of the MPBHXs with/without metal foam is evaluated in Subsection 4.4. Lastly, a parametric study is carried out in Subsection 4.5 to quantify the effects of particle bed capacitance ratio, channel spacing, particle bed mass flow rate, and particle diameter on the heat transfer coefficient and heat transfer rate in the MPBHXs.

4.1. Hypothesis for heat transfer enhancement in metal foam MPBHX

The heat transfer enhancement due to the presence of metal foam in the particle channel of the MPBHX can be attributed to two main factors: (1) the increase in the effective thermal conductivity of the particle bed with the metal foam, and (2) the enhanced interstitial heat transfer between the moving particle bed and the metal foam structure. The effective thermal conductivity of the particle bed without metal foams, $k_{\text{bed,eff}}$, is compared with that of the metal foam structure, $k_{\text{mf,eff}}$ (see expressions in Eqs. (13, 14)) for three ϕ_{mf} in Fig. 6 (a), which explicates the high k_{eff} for metal foams compared to particle bed. Fig. 6 (b) shows the volumetric interstitial (particle bed-metal foam) heat transfer coefficient h_{v} (see Eq. (18)) at different porosities. The high effective thermal conductivity, coupled with the interstitial heat transfer between the metal foams and particle bed flow, substantially enhances heat transfer in the particle channel.

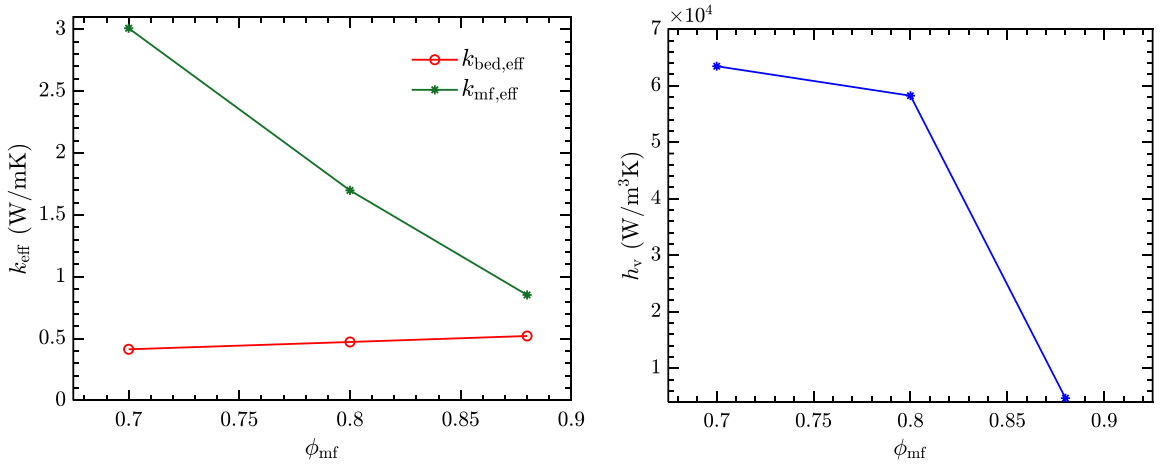

(a) **(b)**

Fig. 6. Variation of (a) effective thermal conductivity and (b) volumetric interstitial heat transfer coefficient as a function of metal foam porosity.

The heat transfer mechanisms from the particle channel to the dividing wall are illustrated in Fig. 7 for the metal foam MPBHX for a representative elementary volume (REV). The primary

heat transfer modes (particle bed conduction, particle bed convection, metal foam conduction, and interstitial heat transfer between particle bed and metal foam) and the typical temperature profiles for the particle channel are also elucidated. Based on the energy balance, the heat flux is transferred to the dividing wall through both the particle bed (q_{bed}) and metal foam (q_{mf}) and then transferred to the sCO$_2$ channel (q_{wg}). So, the sum of q_{bed} and q_{mf} should equal q_{wg} for the proposed model to be valid. The q profiles for the various components and the energy balance are discussed in Subsection 4.2.

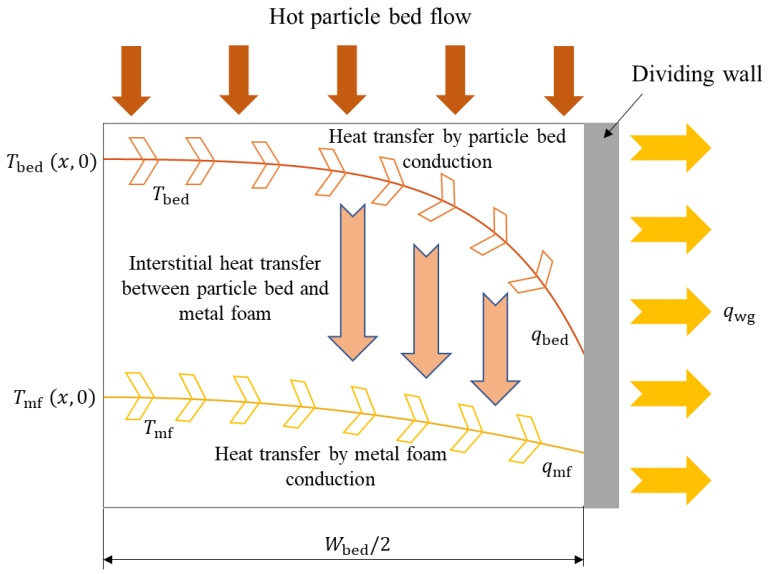

Fig. 7. Schematic of heat transfer mechanisms between particle bed and dividing wall in metal foam MPBHX for a REV.

4.2 Temperature and heat flux profiles

The temperature profiles of the particle bed, metal foam, wall, and sCO$_2$ for the metal foam (ϕ_{mf} = 0.70) and open channel MPBHXs are shown in Fig. 8 (a, b), respectively. The baseline particle bed and metal foam properties used are from Table 8 and Table 4, respectively, in all the simulations, and u_{bed} for open channel/metal foam MPBHXs is the same. The metal foam MPBHX shows higher sCO$_2$ outlet temperatures (703ºC) than the open channel MPBHX (696ºC). It is also observed from Fig. 8 (a, b) that in general the temperature difference between the particle bed and the wall is higher in the case of open channel MPBHX than metal foam MPBHX which implies higher heat transfer for the metal foam MPBHX. The k_{eff} and h_v for the metal foam MPBHX enhance heat transfer in the particle channel and counter the effects of near wall thermal resistance,

which is a significant cause of low heat transfer coefficients in open channel MPBHXs [9,12]. The temperature contours in Fig. 9 (a, b) also indicate greater heat transfer from the particle bed in the metal foam MPBHX which is evident by the presence of the high temperature zone (775ºC – 650ºC) from x/H = 0 – 0.4, whereas for an open channel MPBHX the high temperature zone extends from x/H = 0 – 0.6 showing lower heat transfer from the particle bed.

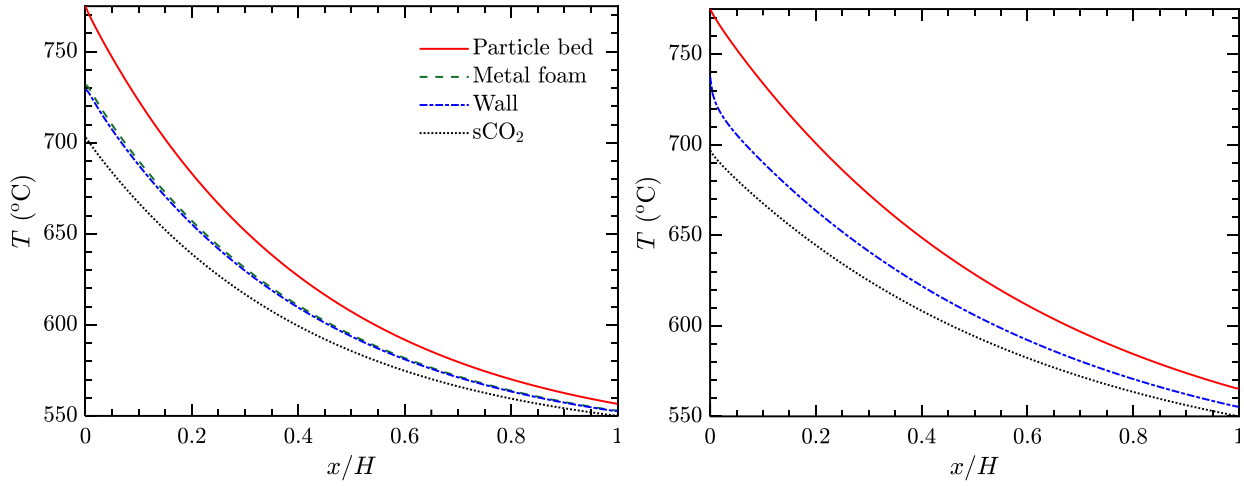

(a) **(b)**

Fig. 8. Temperature profiles of particle bed, metal foam, dividing wall, and sCO_2 along the flow direction for (a) metal foam (ϕ_{mf} = 0.70), and (b) open channel MPBHXs.

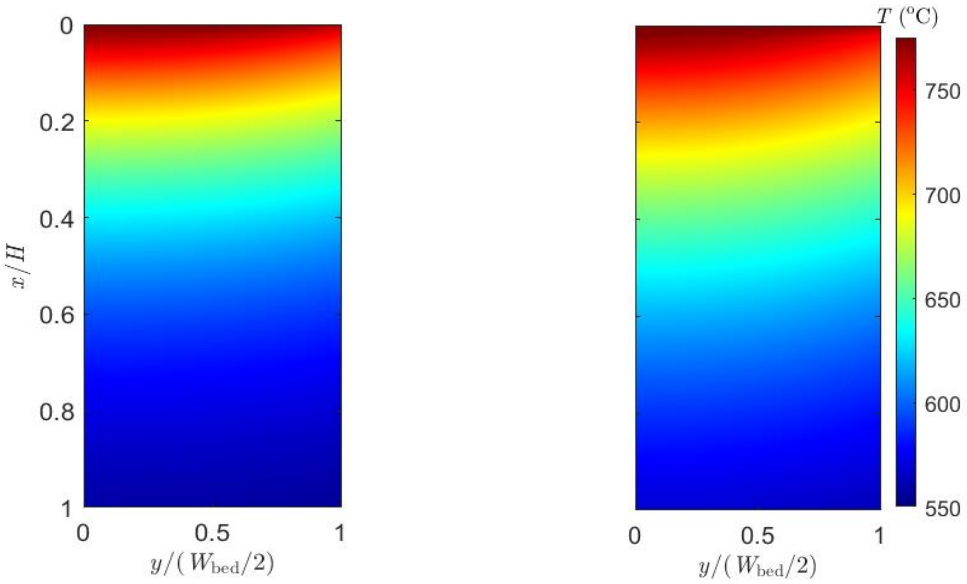

(a) **(b)**

Fig. 9. Temperature contours of particle bed for (a) metal foam (ϕ_{mf} = 0.70), and (b) open channel MPBHXs.

From the steady-state temperature distributions, the local heat flux profiles (q_{bed}, q_{mf}, and q_{wg} defined in Eqs. 5 (a-c) in Table 2) are obtained for the metal foam MPBHX (ϕ_{mf} = 0.70) and presented in Fig. 10 (a). At the particle bed inlet region, there is a slight discrepancy between q_{bed} + q_{mf} and q_{wg}, which is attributed to the grid resolution in the streamwise direction, where a high grid resolution is necessary to resolve the sharp flux gradient at the particle bed inlet region for the metal foam MPBHX. Therefore, from an energy balance perspective, both flux components (q_{bed} + q_{mf} and q_{wg}) should have minimal or no difference for the proposed model/hypothesis to hold. To this end, the grid size in the x-direction is varied (N_y = 64), and the average heat flux ($\bar{q}$) values are presented in Fig. 10 (b). The relative error (R.E.) between $\bar{q}_{bed} + \bar{q}_{mf}$ and $\bar{q}_{wg}$ is defined as

$$\text{R.E.} = \left| \frac{\bar{q}_{bed} + \bar{q}_{mf} - \bar{q}_{wg}}{\bar{q}_{bed} + \bar{q}_{mf}} \right| \tag{28}$$

It can be observed from Fig. 10 (b) that the R.E. between the $\bar{q}_{bed} + \bar{q}_{mf}$ and $\bar{q}_{wg}$ is about 6.13×10^{-5} at a grid size of 2048×64. This low R.E. in the $\bar{q}$ components proves our hypothesis from an energy balance perspective. Furthermore, it shows the effect of N_x on the q behavior, and a grid size of 2048×64 is used for the metal foam MPBHX in the remaining simulations.

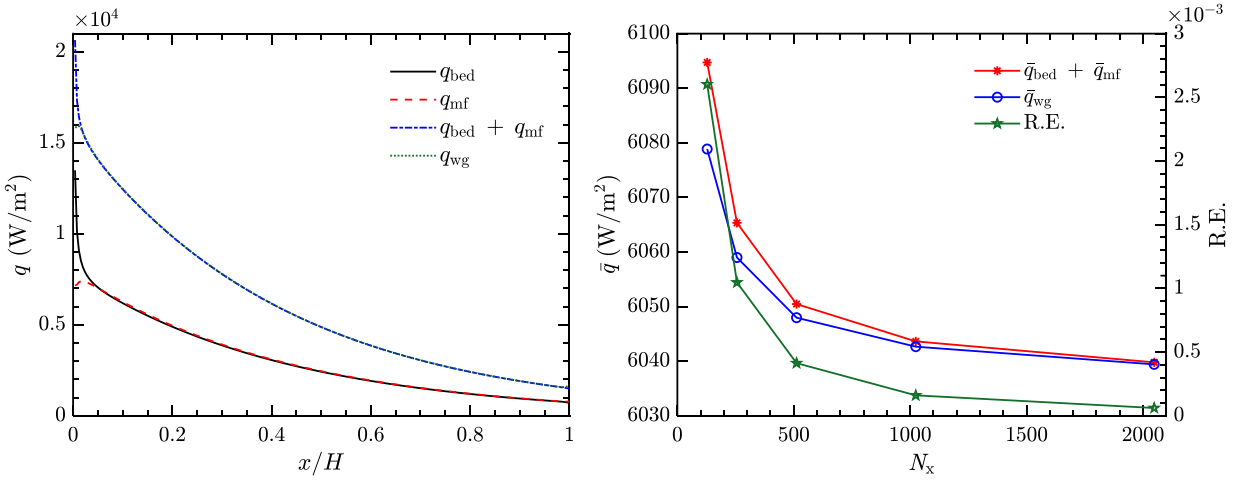

(a) **(b)**

Fig. 10. (a) Comparison of q components along the flow direction and (b) averaged heat flux $\bar{q}$ and relative error versus grid number in the x-direction for the baseline metal foam MPBHX (ϕ_{mf} = 0.70).

The q profile components for the particle channel are shown in Fig. 11(a, b), where for the open channel MPBHX, heat transfer only occurs via particle bed-to-wall, whereas in the metal foam MPBHX, there is an additional heat transfer component from metal foam-to-wall. The q components are high at the thermal entry region (x/H = 0) and decrease further down the channel due to the heat exchange process with sCO_2.

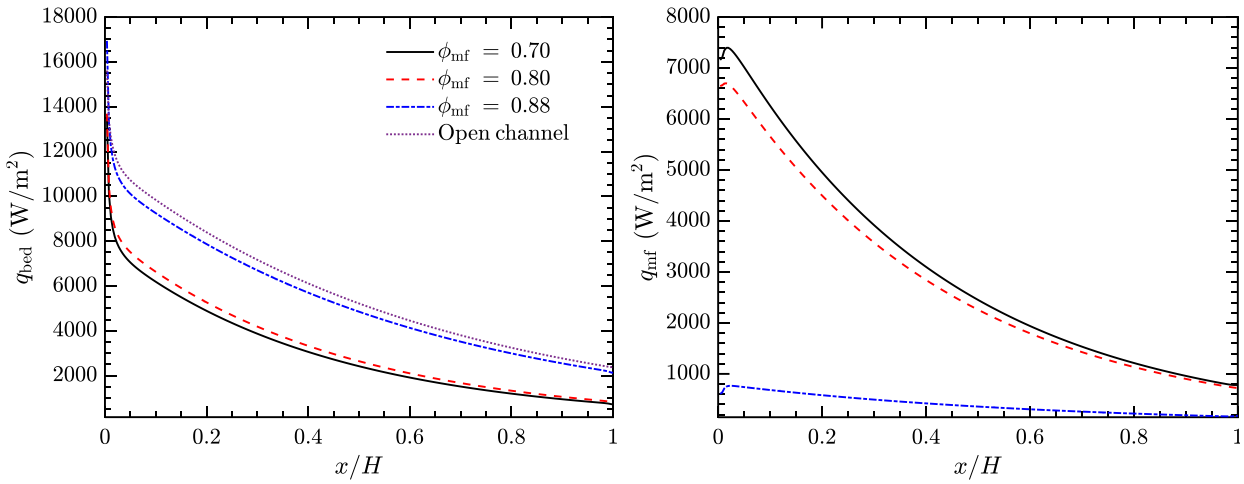

(a) **(b)**

Fig. 11. The local heat flux profiles (a) q_{bed} and (b) q_{mf} in the particle channel for metal foam and open channel MPBHXs.

4.3. Particle bed-to-wall heat transfer coefficient

The $h_{bed,w}$ along the streamwise direction for the four MPBHX configurations (ϕ_{mf} = 0.70, ϕ_{mf} = 0.80, ϕ_{mf} = 0.88, and open channel) is obtained from Eq. (22) and shown in Fig. 12. The presence of metal foam in the particle channel significantly enhances the $h_{bed,w}$ for ϕ_{mf} = 0.70 and 0.8 whereas a small increase is observed for ϕ_{mf} = 0.88. The $h_{bed,w}$ profiles for the metal foam MPBHXs have a similar trend and higher magnitude compared to that for the open channel MPBHX reported by Albrecht and Ho [12] and Yin et al. [60]. An enhanced $h_{bed,w}$ is observed at the thermal entry region, asymptotes to a constant value further down the channel when the flow is thermally developed due to a plug flow assumption for the particle bed flow. Local disturbances in particle bed velocities due to the presence of metal foam may change the behavior of the $h_{bed,w}$ profile, which requires actual flow visualization experiments (e.g., particle velocimetry) [65] or investigation of local flow fields using discrete element modeling (DEM) [66], which would provide in-depth information about the actual particle bed flow field and is beyond the scope of this work.

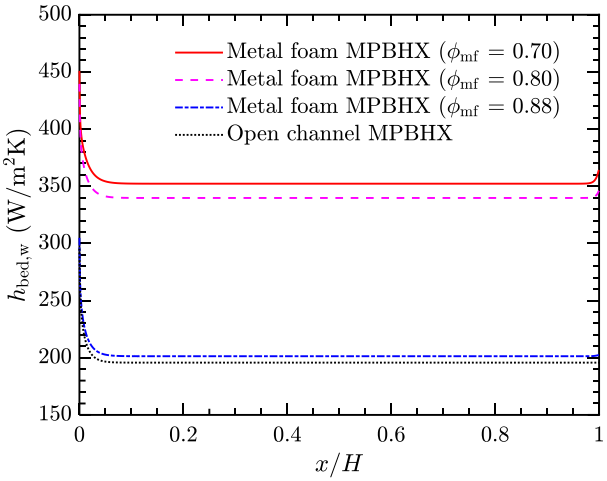

Fig. 12. Comparison of $h_{bed,w}$ along the flow direction for metal foam and open channel MPBHXs.

4.4. Heat transfer performance of MPBHXs

The heat transfer performance of MPBHXs is obtained using Eqs. (23-26) for a heat transfer area of 1 m^2 and summarized in Table 9. The presence of metal foam in the particle channel enhances the heat transfer performance compared to an open channel MPBHX with the $\bar{h}_{bed,w}$ increased by 63% and the U increased by 50% (ϕ_{mf} = 0.70). The ΔT_{LMTD} is also compared between the four configurations where a lower LMTD is observed for the metal foam MPBHX compared to open channel MPBHX due to the metal foam enhancing heat transfer from the particle bed to sCO_2 which is evident by lower particle bed outlet temperature and higher sCO_2 outlet temperatures as observed in Fig. 8. The reduction in particle bed outlet temperature and increase in sCO_2 outlet temperature for the metal foam cases compared to open channel MPBHX case causes a decrease in the ΔT_{LMTD} based on Eq. (26). A similar behavior is also observed for decrease in ΔT_{LMTD} as the ϕ_{mf} decreases and is attributed to the enhanced thermal performance at lower ϕ_{mf} for metal foam MPBHX. The particle selection plays an essential part in enhancing the overall heat transfer, as observed by the difference in the heat transfer metrics shown in Table 10 between the CARBOBEAD particles (thermophysical properties provided in Table 11) and the sintered bauxite particles used in the present study for open channel MPBHX. Compared to sintered bauxite particles, an increase of 10% for the $\bar{h}_{bed,w}$ and 8% for the U for the CARBOBEAD particle is observed, which is attributed to a higher k_p for CARBOBEAD particles compared to sintered bauxite particles.

Table. 9. Heat transfer performance comparison between open channel and metal foam MPBHXs (heat transfer area 1 m^2).

Metrics	Open channel MPBHX	Metal foam MPBHX (ϕ_{mf} = 0.70)	Metal foam MPBHX (ϕ_{mf} = 0.80)	Metal foam MPBHX (ϕ_{mf} = 0.88)
$\bar{h}_{bed,w}$ (W/m^{2}K)	196.41	353.32	340.72	202.29
U (W/m^{2}K)	147.66	221.38	216.36	150.82
LMTD	39.22	27.88	28.43	38.99
Q (W)	5792.51	6172.59	6153.31	5881.76

Table. 10. Heat transfer performance comparison with different particle types selection for the open channel MPBHX (heat transfer area 1 m^2).

Metrics	Bauxite	CARBOBEAD
$\bar{h}_{bed,w}$ (W/m^{2}K)	196.41	216.34
U (W/m^{2}K)	147.66	158.64
LMTD	39.22	36.56
Q (W)	5792.51	5800.50

Table 11. Thermophysical properties of CARBOBEAD particles*.

Parameter	Value
ρ_p (kg/m^3)	3270
$c_{p,p}$ (J/kgK)	1150
k_p (W/mK)	4.5
d_p (m)	250×10^{-6}

*****Particle thermophysical properties obtained from Chung et al. [67] and evaluated at mean of the particle bed and sCO_2 inlet temperatures (662.5ºC).

4.5. Parametric study of the effects of MPBHX design and operating parameters

4.5.1. Effect of heat capacitance ratio

The effect of the heat capacitance ratio $\left(C = \dot{m}_{bed} c_{p,bed} / \dot{m}_{sCO_2} c_{p,sCO_2}\right)$ on the average bed-to-wall heat transfer coefficient, $\bar{h}_{bed,w}$ and overall heat transfer rate Q, defined in Eqs. (23, 25) respectively in Table 6, is investigated for three modes of operation (C = 1.5, C = 1, and C = 0.5 1) for metal

foam and open channel MPBHXs in Fig. 13, where the mass flow rate of the particle bed is kept constant. It can be observed from Fig. 13 (a) that the change in the C has a negligible effect on the $\bar{h}_{\mathrm{bed,w}}$ for various metal foam porosities. While the results in Fig. 13 (b) show that higher Q is achieved with lower C values. This is due to the low Q extraction by the WF from the particle channel in the C = 1.5 case, where the thermal capacity of the hot side is significantly high. Whereas for C = 0.5, the WF has a higher thermal extraction capacity and can extract higher Q from the particle channel. The temperature contours for varying C are illustrated in Fig. 14 (a-c), where a higher particle bed temperature is observed for C = 1.5, and the heat extraction from the WF is elucidated as C decreases in Fig. 14 (b, c), where the WF inlet temperature effect becomes more noticeable.

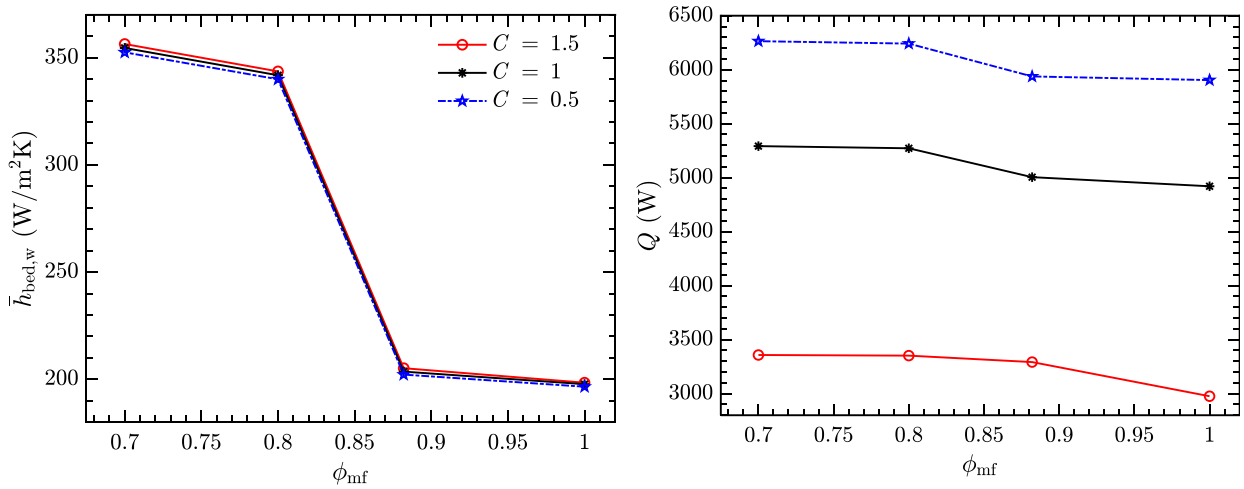

(a) **(b)**

Fig. 13. Variation of (a) $\bar{h}_{\mathrm{bed,w}}$ and (b) Q as a function of C (ϕ_{mf} = 1 refers to open channel MPBHX).

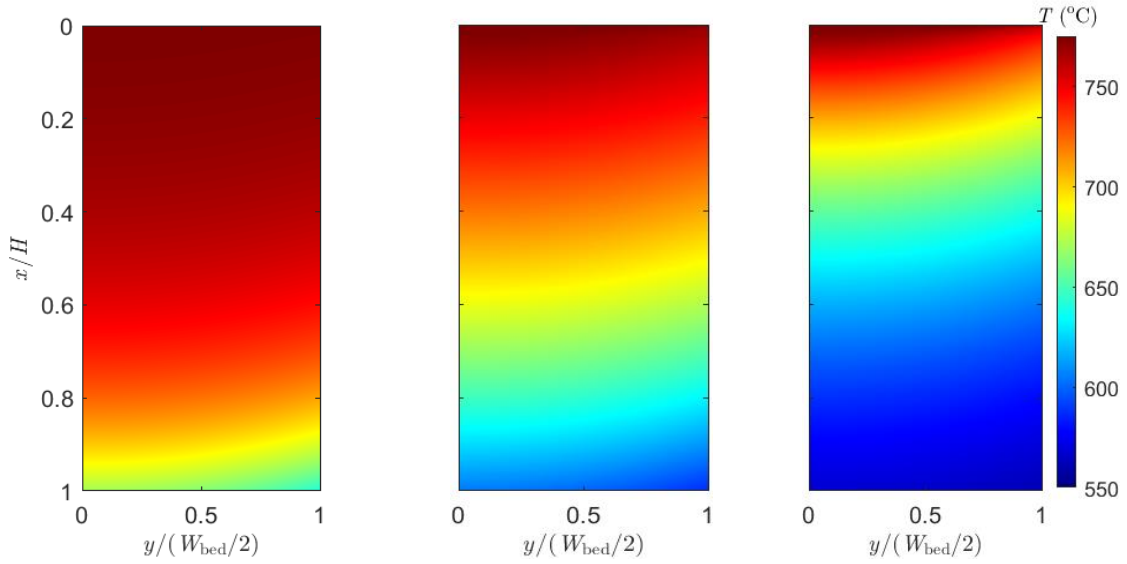

(a) **(b)** **(c)**

Fig. 14. Particle bed temperature contours for (a) *C* = 1.5, (b) *C* = 1 and (c) *C* = 0.5 for metal foam MPBHX (ϕ_{mf} = 0.70).

4.5.2. Effect of particle bed mass flow rate

The particle bed mass flow rate is varied from 16.6 g/s to 75 g/s [12,68] to observe the effects on the heat transfer performance of the MPBHXs. The particle bed mass flow rate significantly increases the heat transfer enhancement in the metal foam channel because h_v is a function of the particle bed mass flow rate/Reynolds number. A higher h_v due to high particle bed mass flow rate increases the particle bed/metal foam interstitial heat transfer, which correlates to higher $\bar{h}_{bed,w}$ and Q, as seen in Fig. 15. For ϕ_{mf} = 0.70 & 0.80, it is observed that the $\bar{h}_{bed,w}$ values keep increasing with increase in the particle bed mass flow rates. In contrast, for ϕ_{mf} = 0.88 and the open channel case, the $\bar{h}_{bed,w}$ values increase and converge at a mass flow rate of 40 g/s. The Q for all the cases appears to converge at a mass flow rate of 70 g/s as the MPBHX approaches its maximum effectiveness. The increase in particle bed temperature due to the increase in particle bed mass flow rate can be observed in Fig. 16, where at 16.6 g/s, a majority of the particle channel remains at the WF inlet temperature, and at 68.6 g/s, the particle bed inlet temperature dominates.

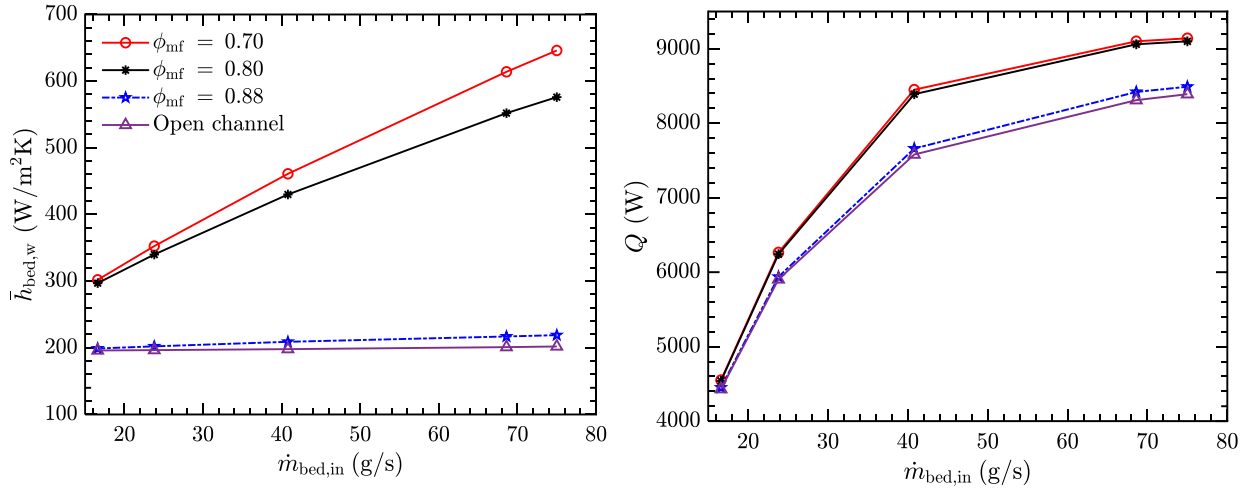

Fig. 15. Variation of (a) $\bar{h}_{bed,w}$ and (b) Q as a function of $\dot{m}_{bed,in}$.

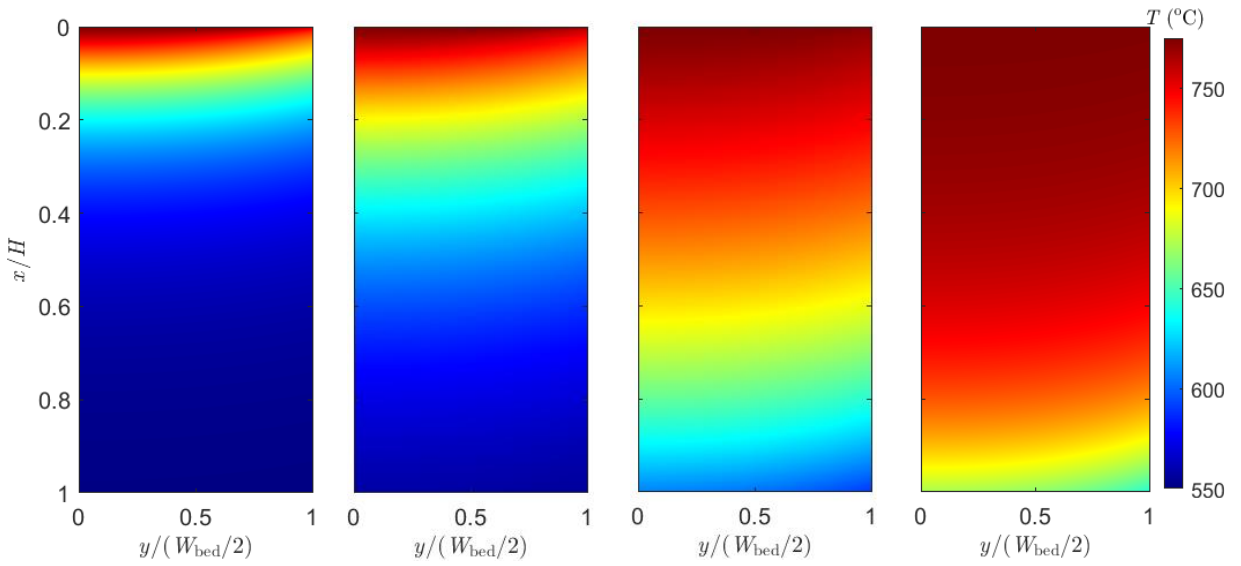

Fig. 16. Particle bed temperature contours for $\dot{m}_{bed,in}$ of (a) 16.6 g/s, (b) 23.8 g/s, (c) 40.8 g/s, and (d) 68.6 g/s for metal foam MPBHX (ϕ_{mf} = 0.70).

4.5.3. Effect of particle bed channel spacing

The particle bed channel spacing is varied from 3 mm to 9 mm [12,13], and the heat transfer performance of the MPBHXs is elucidated in Fig. 17 (a, b), where the $\bar{h}_{bed,w}$ and Q decrease with the increasing particle bed channel spacing because high particle bed channel spacing increases the heat transfer diffusion length in the transverse direction and vice versa. Since a majority of the

heat transfer resistance is on the particle side, Albrecht and Ho [12] and Fang et al. [14] recommended using packed bed channels of 3 mm to obtain higher $\bar{h}_{bed,w}$. The presence of metal foams specifically for ϕ_{mf} = 0.70 and 0.80 shows that high $\bar{h}_{bed,w}$ (>300 W/m^{2}K) can be obtained with sizeable particle bed channel spacing (9 mm) as well.

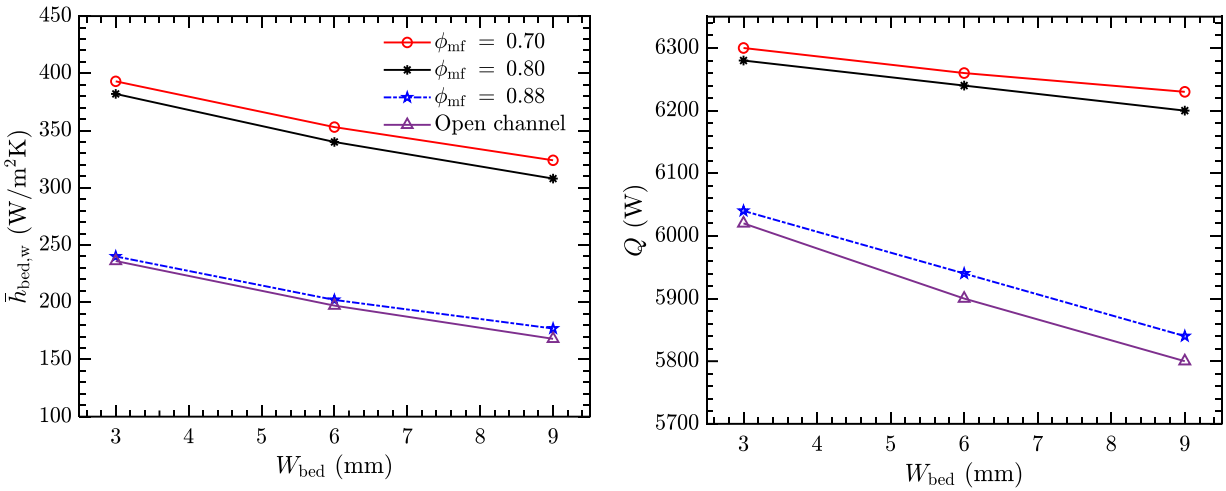

(a) **(b)**

Fig. 17. Variations of (a) $\bar{h}_{bed,w}$ and (b) Q as a function W_{bed}.

4.5.4. Effect of particle diameter

The particle diameter can also play a significant role in the heat transfer and flow behavior of MPBHX and is varied from 100 μm to 750 μm to observe the effects on the heat transfer performance. The present model does not consider the effects of particle radiation as the particle bed thermal conductivity is evaluated based on the model of Yagi and Kunni [58]. The $\bar{h}_{bed,w}$ and Q decrease with an increase in the particle diameter, as seen in Fig. 18 (a, b). This is due to the increased near-wall thermal resistance caused by the increased voidage in the near-wall region. In the particle bed temperature contours shown in Fig. 19 (a, b), the effects of higher near-wall resistance due to large particle diameters become obvious compared to small particle diameters.

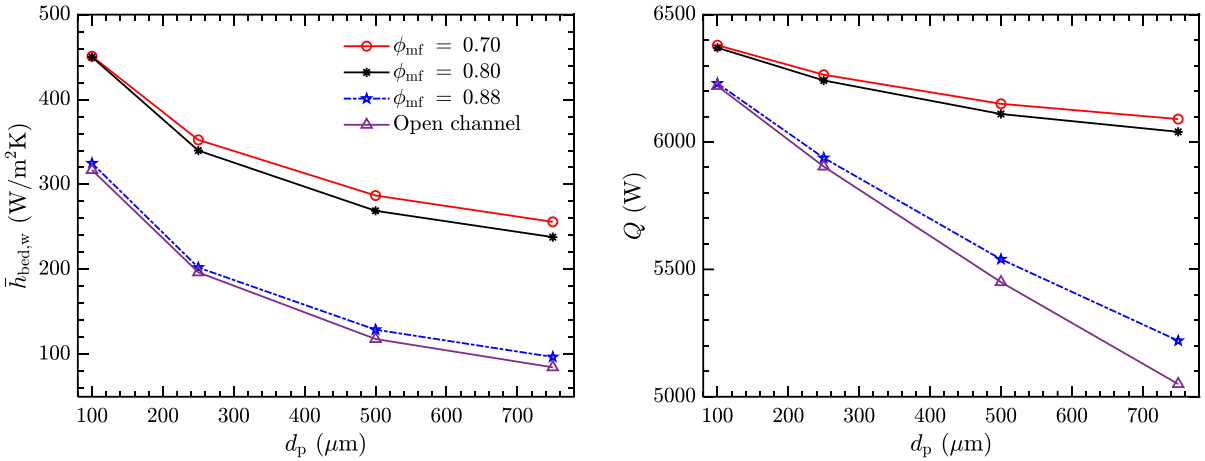

(a) **(b)**

Fig. 18. Variation of (a) $\bar{h}_{bed,w}$ and (b) Q as a function of d_p.

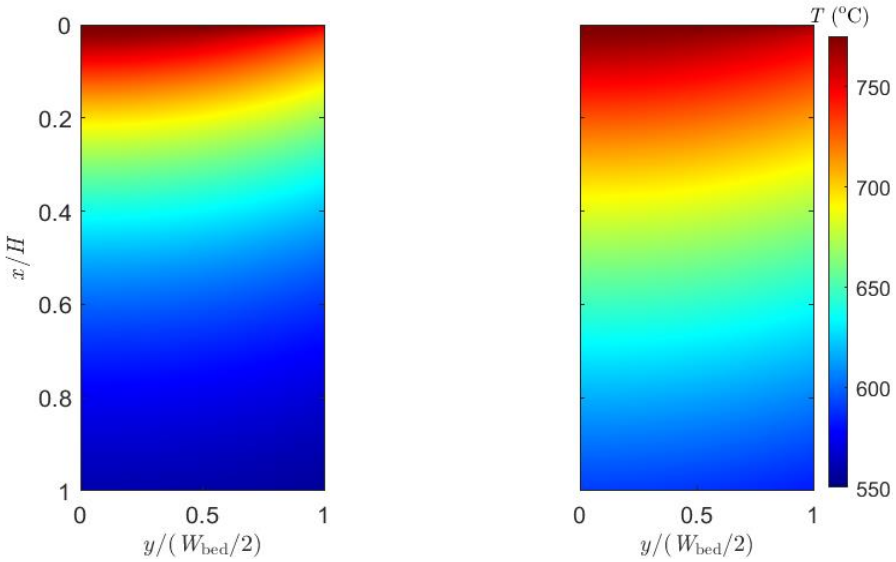

(a) **(b)**

Fig. 19. Particle bed temperature contours for (a) d_p = 100 μm and (b) d_p = 750 μm for the metal foam MPBHX (ϕ_{mf} = 0.88).

5. Conclusions

In this paper, a 2D heat transfer model for counterflow particle-to-sCO_2 MPBHXs with and without metal foams in the particle channel is developed. The numerical model for the open channel HX is verified with analytical solutions in [11] and numerical results in [12], whereas the temperature profiles predicted by the metal foam MPBHX model are verified with the analytical solution for forced convection through metal foams in [53]. The verified model is used to study the thermal enhancement due to the presence of metal foams in the particle channel. The

temperature distributions for the particle bed, dividing wall and sCO_2 stream and heat flux profiles are studied in detail at various metal foam porosities. The particle-to-wall heat transfer coefficient, overall heat transfer coefficient, and total heat transfer are also further determined, and the parametric effects of major MPBHX design and operating parameters on the heat transfer performance of the MPBHX are scrutinized. The following conclusions can be drawn from this study:

- The hypothesis for heat transfer enhancement due to the presence of metal foams where the increased effective thermal conductivity and the interstitial heat transfer are the critical factors for enhanced heat transfer is proposed and verified.
- The heat transfer performance of the open channel and metal foam MPBHXs are compared, where the metal foam MPBHX ($\phi_{mf} = 0.70$) performs better ($\bar{h}_{bed,w} = 352.32$ W/m^{2}K, $U = 221.38$ W/m^{2}K, and $Q = 6.17$ kW for metal foam MPBHX vs $\bar{h}_{bed,w} = 196.41$ W/m^{2}K, $U = 147.66$ W/m^{2}K, and $Q = 5.79$ kW for open channel MPBHX) at baseline operation parameters.
- The particle selection for the MPBHX also plays a vital role as a high intrinsic thermal conductivity of the particle can enhance heat transfer performance ($\bar{h}_{bed,w} = 216.34$ W/m^{2}K, $U = 158.64$ W/m^{2}K, and $Q = 5.8$ kW for CARBOBEAD particles vs $\bar{h}_{bed,w} = 196.41$ W/m^{2}K, $U = 147.66$ W/m^{2}K, and $Q = 5.79$ kW for sintered bauxite particles).
- A detailed parametric study is carried out to determine the effects of critical operating and geometric parameters including heat capacitance ratio, mass flow rate of the particle bed, particle bed channel spacing, and particle diameter, and comparisons are made with and without metal foam for determining $\bar{h}_{bed,w}$ and Q. This gives insights into the parameters selection for designing MPBHXs with metal foams.

The present study can serve as a valuable reference for designing advanced heat exchangers including porous media like metal foams, fins, and tube banks in the particle channel for heat transfer enhancement and optimization, and can be utilized to study transient effects of various operating conditions on MPBHXs. However, although the results for heat transfer enhancement are promising from the present study, further experimental studies are needed to validate the present model; in addition, the model can be improved by incorporating better resolved particle bed flow such as through DEM simulations; furthermore, for particle flows with high flow rates

and large particle diameters, particle clogging may become a significant disadvantage that must be experimentally addressed.

Acknowledgments

This material is based upon work supported by the U.S. Department of Energy's Office of Energy Efficiency and Renewable Energy (EERE) under the Solar Energy Technologies Office Award Number DE-EE0009377.

Nomenclature

Latin letters

d_{fiber}	Metal foam fiber diameter
$\bar{h}$	Average heat transfer coefficient (W/m^{2}K)
A	Area of heat exchanger (m^2)
Bi	Biot number
C	Capacitance ratio
c_{p}	Specific heat capacity (kg/m^3)
d_{p}	Particle Ddiameter (m)
f	Darcy friction factor
h	Heat transfer coefficient (W/m^{2}K)
H	Height (m)
h_{v}	Volumetric interstitial heat transfer coefficient (W/m^{3}K)
k	Thermal conductivity (W/mK)
NTU	Number of transfer units
Nu	Nusselt number
Pr	Prandtl number
q	Heat flux (W/m^2)
Q	Total heat transfer (W)

R	Specific thermal resistance (m^2K/W)
T	Temperature (^oC)
t	Thickness (m)
U	Overall heat transfer coefficient (W/m^2K)
u	Superficial velocity (m/s)
W	Width (m)

Greek letters

μ	Viscosity (kg/ms)
ε_{bed}	Bed porosity
ρ	Density (kg/m^3)
ϕ_{mf}	Metal foam porosity

Subscripts

air	Air
bed	Particle bed
bed,eff	Particle bed effective
bed,w	Particle bed-to-wall
D_h	Hydraulic diameter (m)
fiber	Metal foam fiber
g	sCO_2
LMTD	Log mean temperature difference
mf	Metal foam
mf,eff	Metal foam effective
nw	Near-wall
p	Particle
v	Volumetric
w	Wall
wg	Wall-to-gas

Superscripts

in	Inlet
out	Outlet

Abbreviations

AM	Additively manufactured
CSP	Concentrated solar power
DEM	Discrete element modeling
HTF	Heat transfer fluid
HX	Heat exchanger
LCOE	Levelized cost of electricity
MPBHX	Moving packed bed heat exchanger
PCM	Phase change material
sCO_2	Supercritical carbon dioxide
TES	Thermal energy storage
WF	Working fluid

References

[1] A.G. Olabi, M.A. Abdelkareem, Renewable energy and climate change, Renew. Sustain. Energy Rev. 158 (2022) 112111. https://doi.org/10.1016/j.rser.2022.112111.

[2] M. Ozeh, A. Mishra, X. Wang, Mini wind turbine for small scale power generation and storage (Archimedes wind turbine model), in: ASME Int. Mech. Eng. Congr. Expo. Proc., 2018. https://doi.org/10.1115/IMECE2018-88455.

[3] O. Achkari, A. El Fadar, Latest developments on TES and CSP technologies – Energy and environmental issues, applications and research trends, Appl. Therm. Eng. 167 (2020) 114806. https://doi.org/10.1016/j.applthermaleng.2019.114806.

[4] R. Vakulchuk, I. Overland, D. Scholten, Renewable energy and geopolitics: A review, Renew. Sustain. Energy Rev. 122 (2020) 109547. https://doi.org/10.1016/j.rser.2019.109547.

[5] G.E. Halkos, E.-C. Gkampoura, Reviewing Usage, Potentials, and Limitations of Renewable Energy Sources, Energies. 13 (2020) 2906. https://doi.org/10.3390/en13112906.

[6] S. Pramanik, R.V. Ravikrishna, A review of concentrated solar power hybrid technologies, Appl. Therm. Eng. 127 (2017) 602–637. https://doi.org/10.1016/j.applthermaleng.2017.08.038.

[7] M. Mehos, C. Turchi, J. Vidal, M. Wagner, Z. Ma, C. Ho, W. Kolb, C. Andraka, A. Kruizenga, Concentrating Solar Power Gen3 Demonstration Roadmap, Golden, CO (United States), 2017. https://doi.org/10.2172/1338899.

[8] C.K. Ho, A review of high-temperature particle receivers for concentrating solar power, Appl. Therm. Eng. 109 (2016) 958–969. https://doi.org/10.1016/j.applthermaleng.2016.04.103.

[9] C.K. Ho, M. Carlson, K.J. Albrecht, Z. Ma, S. Jeter, C.M. Nguyen, Evaluation of Alternative Designs for a High Temperature Particle-to-sCO2 Heat Exchanger, J. Sol. Energy Eng. 141 (2019). https://doi.org/10.1115/1.4042225.

[10] C.S. Turchi, Z. Ma, T.W. Neises, M.J. Wagner, Thermodynamic Study of Advanced Supercritical Carbon Dioxide Power Cycles for Concentrating Solar Power Systems, J. Sol. Energy Eng. 135 (2013). https://doi.org/10.1115/1.4024030.

[11] P.A. Isaza, W.D. Warnica, M. Bussmann, Co-current parallel-plate moving bed heat exchanger: An analytical solution, Int. J. Heat Mass Transf. 87 (2015) 616–624. https://doi.org/10.1016/j.ijheatmasstransfer.2015.02.079.

[12] K.J. Albrecht, C.K. Ho, Heat Transfer Models of Moving Packed-Bed Particle-to-sCO2 Heat Exchangers, J. Sol. Energy Eng. 141 (2018). https://doi.org/10.1115/1.4041546.

[13] K.J. Albrecht, C.K. Ho, Design and operating considerations for a shell-and-plate, moving packed-bed, particle-to-sCO2 heat exchanger, Sol. Energy. 178 (2019) 331–340. https://doi.org/10.1016/j.solener.2018.11.065.

[14] W. Fang, S. Chen, J. Xu, K. Zeng, Predicting heat transfer coefficient of a shell-and-plate, moving packed-bed particle-to-sCO2 heat exchanger for concentrating solar power, Energy. 217 (2021) 119389. https://doi.org/10.1016/J.ENERGY.2020.119389.

[15] W. Fang, S. Chen, S. Shi, Dynamic characteristics and real-time control of a particle-to-sCO2 moving bed heat exchanger assisted by BP neural network, Energy. 256 (2022) 124597. https://doi.org/10.1016/j.energy.2022.124597.

[16] K.J. Albrecht, C.K. Ho, High-temperature flow testing and heat transfer for a moving packed-bed particle/sCO2 heat exchanger, AIP Conf. Proc. 2033 (2018). https://doi.org/10.1063/1.5067039.

[17] H.F. Laubscher, K.J. Albrecht, C.K. Ho, High-Temperature Particle Flow Testing in Parallel Plates for Particle-to-Supercritical CO2 Heat Exchanger Applications, in: ASME 2020 14th Int. Conf. Energy Sustain., American Society of Mechanical Engineers, 2020. https://doi.org/10.1115/ES2020-1664.

[18] K.J. Albrecht, M.D. Carlson, H.F. Laubscher, R. Crandell, N. DeLovato, C.K. Ho, Testing and model validation of a prototype moving packed-bed particle-to-sCO2 heat exchanger, in: 2020: p. 030002. https://doi.org/10.1063/5.0031483.

[19] Z. Guo, Z. Tan, X. Tian, Z. Wu, T. Wang, J. Yang, Q. Wang, Heat transfer prediction of granular flow in moving bed heat exchanger: Characteristics of heat transfer enhancement and dynamic control, Sol. Energy. 230 (2021) 1052–1069. https://doi.org/10.1016/J.SOLENER.2021.11.014.

[20] M. Fernández-Torrijos, K.J. Albrecht, C.K. Ho, Dynamic modeling of a particle/supercritical CO2 heat exchanger for transient analysis and control, Appl. Energy. 226 (2018) 595–606. https://doi.org/10.1016/J.APENERGY.2018.06.016.

[21] B. Jiang, D. Xia, H. Guo, L. Xiao, H. Qu, X. Liu, Efficient waste heat recovery system for high-temperature solid particles based on heat transfer enhancement, Appl. Therm. Eng. 155 (2019) 166–174. https://doi.org/10.1016/j.applthermaleng.2019.03.101.

[22] C. Nguyen, D. Sadowski, A. Alrished, H. Al-Ansary, S. Jeter, S. Abdel-Khalik, Study on Solid Particles as a Thermal Medium, Energy Procedia. 49 (2014) 637–646. https://doi.org/10.1016/j.egypro.2014.03.069.

[23] C.E. Christen, J. Gómez-Hernández, T.P. Otanicar, Bimodal particle distributions with increased thermal conductivity for solid particles as heat transfer media and storage materials, Int. J. Heat Mass Transf. 184 (2022) 122250. https://doi.org/10.1016/j.ijheatmasstransfer.2021.122250.

[24] J. Shi, H. Du, Z. Chen, S. Lei, Review of phase change heat transfer enhancement by metal foam, Appl. Therm. Eng. 219 (2023) 119427. https://doi.org/10.1016/j.applthermaleng.2022.119427.

[25] M. Hemmat Esfe, M. Bahiraei, H. Hajbarati, M. Valadkhani, A comprehensive review on convective heat transfer of nanofluids in porous media: Energy-related and thermohydraulic characteristics, Appl. Therm. Eng. 178 (2020) 115487. https://doi.org/10.1016/j.applthermaleng.2020.115487.

[26] W.C. Tan, L.H. Saw, H.S. Thiam, J. Xuan, Z. Cai, M.C. Yew, Overview of porous media/metal foam application in fuel cells and solar power systems, Renew. Sustain. Energy Rev. 96 (2018) 181–197. https://doi.org/10.1016/J.RSER.2018.07.032.

[27] G. Bamorovat Abadi, D.Y. Kim, S.Y. Yoon, K.C. Kim, Thermal performance of a 10-kW phase-change plate heat exchanger with metal foam filled channels, Appl. Therm. Eng. 99 (2016) 790–801. https://doi.org/10.1016/j.applthermaleng.2016.01.156.

[28] C. Zhao, M. Opolot, M. Liu, J. Wang, F. Bruno, S. Mancin, K. Hooman, Review of analytical studies of melting rate enhancement with fin and/or foam inserts, Appl. Therm. Eng. 207 (2022) 118154. https://doi.org/10.1016/j.applthermaleng.2022.118154.

[29] A. Mishra, D. Korba, I. Kaur, P. Singh, L. Li, Prediction and Validation of Flow Properties in Porous Lattice Structures, J. Fluids Eng. (2022) 1–61. https://doi.org/10.1115/1.4056524.

[30] P.H. Jadhav, N. Gnanasekaran, D.A. Perumal, M. Mobedi, Performance evaluation of partially filled high porosity metal foam configurations in a pipe, Appl. Therm. Eng. 194 (2021) 117081. https://doi.org/10.1016/j.applthermaleng.2021.117081.

[31] P.H. Jadhav, T. G, N. Gnanasekaran, M. Mobedi, Performance score based multi-

objective optimization for thermal design of partially filled high porosity metal foam pipes under forced convection, Int. J. Heat Mass Transf. 182 (2022) 121911. https://doi.org/10.1016/j.ijheatmasstransfer.2021.121911.

[32] M. Ghaneifar, H. Arasteh, R. Mashayekhi, A. Rahbari, R. Babaei Mahani, P. Talebizadehsardari, Thermohydraulic analysis of hybrid nanofluid in a multilayered copper foam heat sink employing local thermal non-equilibrium condition: Optimization of layers thickness, Appl. Therm. Eng. 181 (2020) 115961. https://doi.org/10.1016/j.applthermaleng.2020.115961.

[33] J.M. Mahdi, H.I. Mohammed, P. Talebizadehsardari, M. Ghalambaz, H. Sh. Majdi, A. Khan, W. Yaïci, D. Giddings, Simultaneous and consecutive charging and discharging of a PCM-based domestic air heater with metal foam, Appl. Therm. Eng. 197 (2021) 117408. https://doi.org/10.1016/j.applthermaleng.2021.117408.

[34] Q. Ying, H. Wang, E. Lichtfouse, Numerical simulation on thermal behavior of partially filled metal foam composite phase change materials, Appl. Therm. Eng. 229 (2023) 120573. https://doi.org/10.1016/j.applthermaleng.2023.120573.

[35] S. De Schampheleire, P. De Jaeger, R. Reynders, K. De Kerpel, B. Ameel, C. T'Joen, H. Huisseune, S. Lecompte, M. De Paepe, Experimental study of buoyancy-driven flow in open-cell aluminium foam heat sinks, Appl. Therm. Eng. 59 (2013) 30–40. https://doi.org/10.1016/j.applthermaleng.2013.05.010.

[36] W. He, X. Liu, R. Qiu, Y. Zhuang, C. Wang, Z. Li, A comprehensive approach combining gradient porous metal foam and the magnetic field to regulate latent heat storage performance, Appl. Therm. Eng. 227 (2023) 120380. https://doi.org/10.1016/j.applthermaleng.2023.120380.

[37] C.Y. Zhao, W. Lu, Y. Tian, Heat transfer enhancement for thermal energy storage using metal foams embedded within phase change materials (PCMs), Sol. Energy. 84 (2010) 1402–1412. https://doi.org/10.1016/j.solener.2010.04.022.

[38] L. Liang, Y.H. Diao, Y.H. Zhao, Z.Y. Wang, F.W. Bai, Numerical and experimental investigations of latent thermal energy storage device based on a flat micro-heat pipe array–metal foam composite structure, Renew. Energy. 161 (2020) 1195–1208. https://doi.org/10.1016/j.renene.2020.07.033.

[39] C.Y. Zhao, Z.G. Wu, Heat transfer enhancement of high temperature thermal energy storage using metal foams and expanded graphite, Sol. Energy Mater. Sol. Cells. 95 (2011) 636–643. https://doi.org/10.1016/j.solmat.2010.09.032.

[40] H. Tian, T. Zhao, L. Shi, T. Chen, X. Ma, H. Zhang, G. Shu, Assessment and optimization of exhaust gas heat exchanger with porous baffles and porous fins, Appl. Therm. Eng. 178 (2020) 115446. https://doi.org/10.1016/j.applthermaleng.2020.115446.

[41] F. Alawwa, M. Saeed, R. Homsi, H. Zhu, A.S. Berrouk, M. Khalil, G. Xie, Y. Al Wahedi, Thermohydraulic performance comparison of 3D printed circuit heatsinks with conventional integral fin heatsinks, Appl. Therm. Eng. 226 (2023) 120356. https://doi.org/10.1016/j.applthermaleng.2023.120356.

[42] J. Guo, Z. Liu, Z. Du, J. Yu, X. Yang, J. Yan, Effect of fin-metal foam structure on thermal energy storage: An experimental study, Renew. Energy. 172 (2021) 57–70. https://doi.org/10.1016/j.renene.2021.03.018.

[43] S. Saedodin, S.A.H. Zamzamian, M.E. Nimvari, S. Wongwises, H.J. Jouybari, Performance evaluation of a flat-plate solar collector filled with porous metal foam: Experimental and numerical analysis, Energy Convers. Manag. 153 (2017) 278–287. https://doi.org/10.1016/j.enconman.2017.09.072.

[44] I. Kaur, Y. Aider, K. Nithyanandam, P. Singh, Thermal-hydraulic performance of additively manufactured lattices for gas turbine blade trailing edge cooling, Appl. Therm. Eng. 211 (2022) 118461. https://doi.org/10.1016/j.applthermaleng.2022.118461.

[45] N. Wang, I. Kaur, P. Singh, L. Li, Prediction of effective thermal conductivity of porous lattice structures and validation with additively manufactured metal foams, Appl. Therm. Eng. 187 (2021) 116558. https://doi.org/10.1016/J.APPLTHERMALENG.2021.116558.

[46] I. Kaur, P. Singh, Flow and Thermal Transport Through Unit Cell Topologies of Cubic and Octahedron Families, Int. J. Heat Mass Transf. 158 (2020) 119784. https://doi.org/10.1016/J.IJHEATMASSTRANSFER.2020.119784.

[47] Y. Aider, I. Kaur, A. Mishra, L. Li, H. Cho, J. Martinek, Z. Ma, P. Singh, Heat Transfer Characteristics of Particle and Air Flow Through Additively Manufactured Lattice Frame Material Based on Octet-Shape Topology, J. Sol. Energy Eng. 145 (2023). https://doi.org/10.1115/1.4062196.

[48] Y. Aider, A. Mishra, L. Li, H. Cho, P. Singh, Heat Transfer Characteristics of Particle Flow Through Additively Manufactured (SS 316L) Lattice Frame Material Based on Octet-Shape Topology, in: Vol. 8 Fluids Eng. Heat Transf. Therm. Eng., American Society of Mechanical Engineers, 2022. https://doi.org/10.1115/IMECE2022-95962.

[49] C.K. Ho, K.J. Albrecht, L. Yue, B. Mills, J. Sment, J. Christian, M. Carlson, Overview and design basis for the Gen 3 Particle Pilot Plant (G3P3), in: 2020: p. 030020. https://doi.org/10.1063/5.0029216.

[50] T. Baumann, S. Zunft, Development and Performance Assessment of a Moving Bed Heat Exchanger for Solar Central Receiver Power Plants, Energy Procedia. 69 (2015) 748–757. https://doi.org/10.1016/j.egypro.2015.03.085.

[51] J.-M. Yin, Q.-Y. Zheng, X.-R. Zhang, Comparative study on the thermal-hydraulic performance of a shell and plate particle-SCO2 moving packed bed heat exchanger with various channel configurations, Appl. Therm. Eng. 181 (2020) 115946. https://doi.org/10.1016/j.applthermaleng.2020.115946.

[52] V. V. Calmidi, R.L. Mahajan, Forced Convection in High Porosity Metal Foams, J. Heat Transfer. 122 (2000) 557–565. https://doi.org/10.1115/1.1287793.

[53] D.-Y. Lee, K. Vafai, Analytical characterization and conceptual assessment of solid and fluid temperature differentials in porous media, Int. J. Heat Mass Transf. 42 (1999) 423–435. https://doi.org/10.1016/S0017-9310(98)00185-9.

[54] A.S. Suleiman, N. Dukhan, Forced convection inside metal foam: Simulation over a long

domain and analytical validation, Int. J. Therm. Sci. 86 (2014) 104–114. https://doi.org/10.1016/J.IJTHERMALSCI.2014.06.022.

[55] R. Span, W. Wagner, A New Equation of State for Carbon Dioxide Covering the Fluid Region from the Triple-Point Temperature to 1100 K at Pressures up to 800 MPa, J. Phys. Chem. Ref. Data. 25 (1996) 1509–1596. https://doi.org/10.1063/1.555991.

[56] V. Vesovic, W.A. Wakeham, G.A. Olchowy, J. V. Sengers, J.T.R. Watson, J. Millat, The Transport Properties of Carbon Dioxide, J. Phys. Chem. Ref. Data. 19 (1990) 763–808. https://doi.org/10.1063/1.555875.

[57] J.S.M. Botterill, A.O.O. Denloye, A theoretical model of heat transfer to a packed or quiescent fluidized bed, Chem. Eng. Sci. 33 (1978) 509–515. https://doi.org/10.1016/0009-2509(78)80011-6.

[58] S. Yagi, D. Kunii, Studies on effective thermal conductivities in packed beds, AIChE J. 3 (1957) 373–381. https://doi.org/10.1002/aic.690030317.

[59] A.O.O. Denloye, J.S.M. Botterill, Heat transfer in flowing packed beds, Chem. Eng. Sci. 32 (1977) 461–465. https://doi.org/10.1016/0009-2509(77)87001-2.

[60] J.-M. Yin, Q.-Y. Zheng, X.-R. Zhang, Heat transfer model of a particle energy storage-based moving packed bed heat exchanger, Energy Storage. 2 (2020) e113. https://doi.org/https://doi.org/10.1002/est2.113.

[61] GNIELINSKI, V., New Equations for Heat and Mass Transfer in Turbulent Pipe and Channel Flow, Int. Chem. Eng. 16 (1976) 359–368. http://ci.nii.ac.jp/naid/10024351277/en/ (accessed March 8, 2022).

[62] F.P. Incropera, Fundamentals of Heat and Mass Transfer, John Wiley & Sons, Inc., Hoboken, NJ, USA, 2006.

[63] S.-C. Tzeng, T.-M. Jeng, Interstitial Heat Transfer Coefficient and Dispersion Conductivity in Compressed Metal Foam Heat Sinks, J. Electron. Packag. 129 (2007) 113–119. https://doi.org/10.1115/1.2721081.

[64] N.-S. Cheng, A.W.-K. Law, Exponential formula for computing effective viscosity, Powder Technol. 129 (2003) 156–160. https://doi.org/10.1016/S0032-5910(02)00274-7.

[65] P. Bartsch, S. Zunft, Granular flow around the horizontal tubes of a particle heat exchanger: DEM-simulation and experimental validation, Sol. Energy. 182 (2019) 48–56. https://doi.org/10.1016/J.SOLENER.2019.01.086.

[66] X. Tian, J. Yang, Z. Guo, Q. Wang, Numerical investigation of gravity-driven granular flow around the vertical plate: Effect of pin-fin and oscillation on the heat transfer†, Energies. 14 (2021) 2187. https://doi.org/10.3390/en14082187.

[67] K.M. Chung, J. Zeng, S.R. Adapa, T. Feng, M. V. Bagepalli, P.G. Loutzenhiser, K.J. Albrecht, C.K. Ho, R. Chen, Measurement and analysis of thermal conductivity of ceramic particle beds for solar thermal energy storage, Sol. Energy Mater. Sol. Cells. 230 (2021) 111271. https://doi.org/10.1016/j.solmat.2021.111271.

[68] J.-M. Yin, Q.-Y. Zheng, X.-R. Zhang, Dynamic characteristics of a shell and plate particle-SCO2 moving packed bed heat exchanger with various SCO2 channel configurations, Int. J. Energy Res. n/a (2020). https://doi.org/https://doi.org/10.1002/er.6290.